Article

Neuron

Xenotransplanted Human Cortical Neurons Reveal Species-Specific Development and Functional Integration into Mouse Visual Circuits

Graphical Abstract

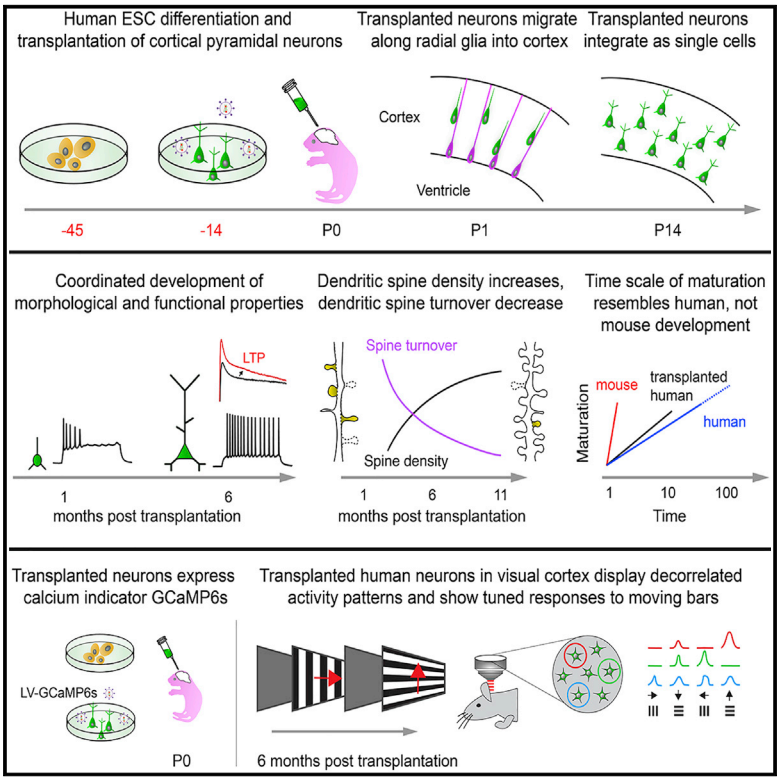

Highlights

- Cell-intrinsic mechanisms of human neoteny in mouse-human chimeric cerebral cortex
- Human neurons show prolonged maturation and single-cell integration in mouse cortex
- Stable dendritic spines and long-term synaptic plasticity in xenotransplanted neurons
- Human neurons show decorrelated activity and tuned responses to visual stimuli

Authors

Daniele Linaro, Ben Vermaercke, Ryohei Iwata, ..., Karl-Klaus Conzelmann, Vincent Bonin, Pierre Vanderhaeghen

Correspondence

vincent.bonin@nerf.be (V.B.), pierre.vanderhaeghen@kuleuven.vib.be (P.V.)

In Brief

Human cortical neurons integrate as single cells in the mouse cortex and display human-like prolonged development, indicating cell-intrinsic mechanisms. Following maturation in the visual cortex, xenotransplanted human neurons display decorrelated activity and tuned responses to visual stimuli that are similar to host neurons.

Linaro et al., 2019, Neuron *104*, 972–986
December 4, 2019
https://doi.org/10.1016/j.neuron.2019.10.002

CellPress

CellPress

Neuron
Article

Xenotransplanted Human Cortical Neurons Reveal Species-Specific Development and Functional Integration into Mouse Visual Circuits

Daniele Linaro,[1,2,3,11] Ben Vermaercke,[1,2,4,11] Ryohei Iwata,[1,2,3,11] Arjun Ramaswamy,[2,4,5] Baptiste Libé-Philippot,[1,2,3] Leila Boubakar,[1,2,3] Brittany A. Davis,[3] Keimpe Wierda,[1] Kristofer Davie,[1] Suresh Poovathingal,[1] Pier-Andrée Penttila,[1] Angéline Bilheu,[3] Lore De Bruyne,[1,2] David Gall,[3,6] Karl-Klaus Conzelmann,[7] Vincent Bonin,[4,5,8,9,12,*] and Pierre Vanderhaeghen[1,2,3,9,10,12,13,*]

[1]VIB-KU Leuven Center for Brain & Disease Research, 3000 Leuven, Belgium
[2]Department of Neurosciences and Leuven Brain Institute, KU Leuven, 3000 Leuven, Belgium
[3]Institut de Recherches en Biologie Humaine et Moléculaire (IRIBHM) and ULB Neuroscience Institute (UNI), Université Libre de Bruxelles (ULB), 1070 Brussels, Belgium
[4]Neuro-Electronics Research Flanders, Kapeldreef 75, 3001 Leuven, Belgium
[5]imec, 3001 Leuven, Belgium
[6]Laboratoire de Physiologie et Pharmacologie and ULB Neuroscience Institute (UNI), Université Libre de Bruxelles (ULB), 1070 Brussels, Belgium
[7]Max von Pettenkofer-Institute and Gene Center, Ludwig-Maximilians-Universität Munchen, 81377 Munich, Germany
[8]Department of Biology and Leuven Brain Institute, KU Leuven, 3000 Leuven, Belgium
[9]VIB, 3000 Leuven, Belgium
[10]Welbio, Université Libre de Bruxelles (ULB), 1070 Brussels, Belgium
[11]These authors contributed equally
[12]Senior author
[13]Lead Contact
*Correspondence: vincent.bonin@nerf.be (V.B.), pierre.vanderhaeghen@kuleuven.vib.be (P.V.)
https://doi.org/10.1016/j.neuron.2019.10.002

SUMMARY

How neural circuits develop in the human brain has remained almost impossible to study at the neuronal level. Here, we investigate human cortical neuron development, plasticity, and function using a mouse/human chimera model in which xenotransplanted human cortical pyramidal neurons integrate as single cells into the mouse cortex. Combined neuronal tracing, electrophysiology, and *in vivo* structural and functional imaging of the transplanted cells reveal a coordinated developmental roadmap recapitulating key milestones of human cortical neuron development. The human neurons display a prolonged developmental timeline, indicating the neuron-intrinsic retention of juvenile properties as an important component of human brain neoteny. Following maturation, human neurons in the visual cortex display tuned, decorrelated responses to visual stimuli, like mouse neurons, demonstrating their capacity for physiological synaptic integration in host cortical circuits. These findings provide new insights into human neuronal development and open novel avenues for the study of human neuronal function and disease.

INTRODUCTION

The brain, and neocortex in particular, increased rapidly in size and complexity during human evolution. While there has been progress in understanding the mechanisms of human cortical expansion, those underlying the assembly of human neurons into complex neural circuits remain poorly understood (Bae et al., 2015; Defelipe, 2011; Geschwind and Rakic, 2013; Lui et al., 2011; Sousa et al., 2017).

A remarkable feature of human cortical circuits, compared with non-human species, is their unusually prolonged development (Petanjek et al., 2011; Rakic et al., 1986). This neoteny, or retention of juvenile traits in a more mature organism, may be critical for the acquisition of human-specific cognitive features (Gould, 1992) and to primarily implicate cortical neurons (Bufill et al., 2011; Defelipe, 2011; Petanjek et al., 2011). The rate of maturation of cortical neurons varies widely across species, most strikingly in the prefrontal cortex, ranging from 5 weeks in the mouse to 4 months in macaque to years in humans. Compared to the macaque neocortex, human cortical neurons display prolonged periods of dendritic morphogenesis and synaptogenesis (over months to several years) and synaptic pruning (up to a decade) (Huttenlocher, 1979; Huttenlocher et al., 1982, 1982–1983; Mrzljak et al., 1990; Petanjek et al., 2011), and comparison with the chimpanzee also indicates human neoteny, although less pronounced (Bianchi et al., 2013; Liu et al., 2012). Beyond evolution, human neoteny has important implications for brain diseases (Liu et al., 2016), as alterations of neuronal maturation are associated with neurodevelopmental disorders (Hutsler and Zhang, 2010; Pfeiffer et al., 2010; Takashima et al., 1981; Willsey et al., 2013).

Despite its importance in brain evolution and diseases, human neuron and synapse development remains poorly known. This is mostly because of the difficulty of studying live human neurons in the context of a brain circuit. Pluripotent stem cell (PSC)-based

models provide new opportunities to study human neural development (Astick and Vanderhaeghen, 2018; Di Lullo and Kriegstein, 2017; Gaspard and Vanderhaeghen, 2010; Suzuki and Vanderhaeghen, 2015; Zeltner and Studer, 2015). However, they have remained difficult to use to study cortical neuron development *in vitro*, given the technical challenges of long-term maintenance of functional neurons, whether as monolayer cultures or in organoids (Di Lullo and Kriegstein, 2017; van den Ameele et al., 2014).

Another approach is xenotransplantation of human neurons into the mouse brain, which can provide a means to study human neuronal maturation under more physiologically realistic conditions. Human PSC-derived pyramidal cortical neurons and interneurons transplanted in the mouse brain develop morphologically and synaptically within their host (Anderson and Vanderhaeghen, 2014; Espuny-Camacho et al., 2013; Maroof et al., 2013; Nicholas et al., 2013; Tornero et al., 2013), and transplanted human neurons develop more slowly than similarly transplanted mouse neurons (Falkner et al., 2016; Gaspard et al., 2008; Michelsen et al., 2015).

Human cortical interneurons have been shown to integrate extensively into the host mouse brain thanks to the remarkable migratory properties of this class of neurons (Cunningham et al., 2014; Fandel et al., 2016; Huo et al., 2018; Noakes et al., 2019; Southwell et al., 2014). However, for pyramidal neurons, it has remained unclear to what extent the transplanted neurons, although competent to make synapses and receive inputs, can integrate physiologically to participate in the function of cortical circuits (Espuny-Camacho et al., 2013, 2017, 2018; Mansour et al., 2018; Qi et al., 2017; Real et al., 2018; Tornero et al., 2017). To date, xenotransplantation studies have focused on cell-compact transplants comprising a large number of cells with limited access to the host tissue; while these transplants are viable and can host vascular and glial cells, they form a local environment that is dramatically different from the host brain and may not provide all of the necessary cues for proper circuit integration. A recent study using *in vivo* imaging showed limited synaptic integration of human cortical pyramidal neurons in the mouse cortex (Real et al., 2018). Likewise, it remains unknown whether the prolonged maturation of transplanted human cortical neurons merely reflects partially isolated graft conditions or it reflects an intrinsic developmental program relevant to human brain neoteny.

Here, we developed a novel experimental model to address these questions, using xenotransplanted human cortical pyramidal neurons that integrate as single cells into the mouse cortex. We show that the transplanted neurons mature following a prolonged human-like timeline, indicating that human neuronal neoteny has a strong intrinsic component. Following maturation, the neurons become highly connected with the host brain and display responses to sensory stimuli that resemble those of host neurons.

RESULTS

Intraventricular Human Cortical Transplantation Leads to Robust Integration in the Mouse Cortex

A major limitation of transplants of cortical pyramidal neurons is that they tend to form poorly integrated lumps in the host tissue. To solve this problem, we performed neural transplantation in the presence of EGTA, which leads to better cell integration in the mouse embryonic cortex (Nagashima et al., 2014), through intraventricular injection into the neonatal brain (Figures 1A and S1A). In these conditions, following injection into the lateral ventricles of the neonatal (P0/P1) mouse brain, human embryonic stem cell (ESC)-derived cortical cells examined 6 h post-transplantation were found attached to or partially invading the surface of the ventricular zone. At 24 h, transplanted cells were found within the cortical tissue and appeared to migrate along the radial glia processes still present at this stage (Figure S1). Transplantation of GFP^+ human neurons into transgenic mice in which tdTomato is expressed in pyramidal neurons revealed no GFP/tdTomato double-positive cells (0 of 40 cells examined by confocal microscopy, n = 2 animals) (Figure S1), indicating the absence of transplant-to-host cell fusion events (Ying et al., 2002). This was further confirmed by single cell RNA sequencing (scRNA-seq) profiling of transplanted cells, which revealed no detectable mouse sequence reads in any of the human cells (n = 10,698 cells, n = 2 animals) (Figure S1).

From 2 weeks to 11 months post-transplantation (MPT), transplanted neurons were found within the cortical gray matter, from deep (5/6) to superficial (2/3) cortical layers, generally displaying radial orientation (Figures 1B and S1B). None of the cells expressed markers of glial cells (0 of 19 cells, n = 2 animals) or GABAergic neurons (0 of 27 cells, n = 2 animals) (Figures 1C, 1D, S1C, and S1D). The majority of cells (>60%) expressed markers of deep cortical layer identity (FoxP2/CTIP2) and were located primarily in layer 5/6 (L5/6), although some were found in L2/3. A minority of cells expressed upper-layer marker Cux1, and these were found exclusively in L2/3. Thus, there was only a partial link between layer identity and positioning of the transplanted neurons (Figure S1).

Transsynaptic rabies experiments were performed to probe the presynaptic partners of human neurons. We used lentivirus infection to express TVA-mCherry and rabies glycoprotein in human neurons *in vitro*, which was performed 2 weeks ahead of transplantation to prevent host infection (Figure S1). To label presynaptic partners, GFP-expressing rabies virus was injected in the cortex of transplanted animals at 4 MPT. This revealed that TVA^+/GFP^+ human neurons (starter cells) were typically surrounded by TVA^-/GFP^+ retrogradely labeled mouse cortical neurons (Figure 1E), suggesting significant connectivity between transplanted and host cortical neurons.

Coordinated Functional and Morphological Neotenic Development of Human Cortical Neurons

To study the functional development of xenotransplanted human neurons, we performed *ex vivo* whole-cell patch-clamp recordings at different time points between 1 and 11 MPT (Figures 2 and S2; Table S1). We observed a progressive maturation of human neurons, starting at 1 MPT with immature physiological properties, such as low-amplitude action potentials (APs) and rapidly adapting responses to current stimulation (Figure 2A). By 10 MPT, the neurons displayed sustained firing and mature-looking APs that closely resemble those of mature human pyramidal neurons (Beaulieu-Laroche et al., 2018; Testa-Silva et al., 2014). These changes were accompanied by progressive

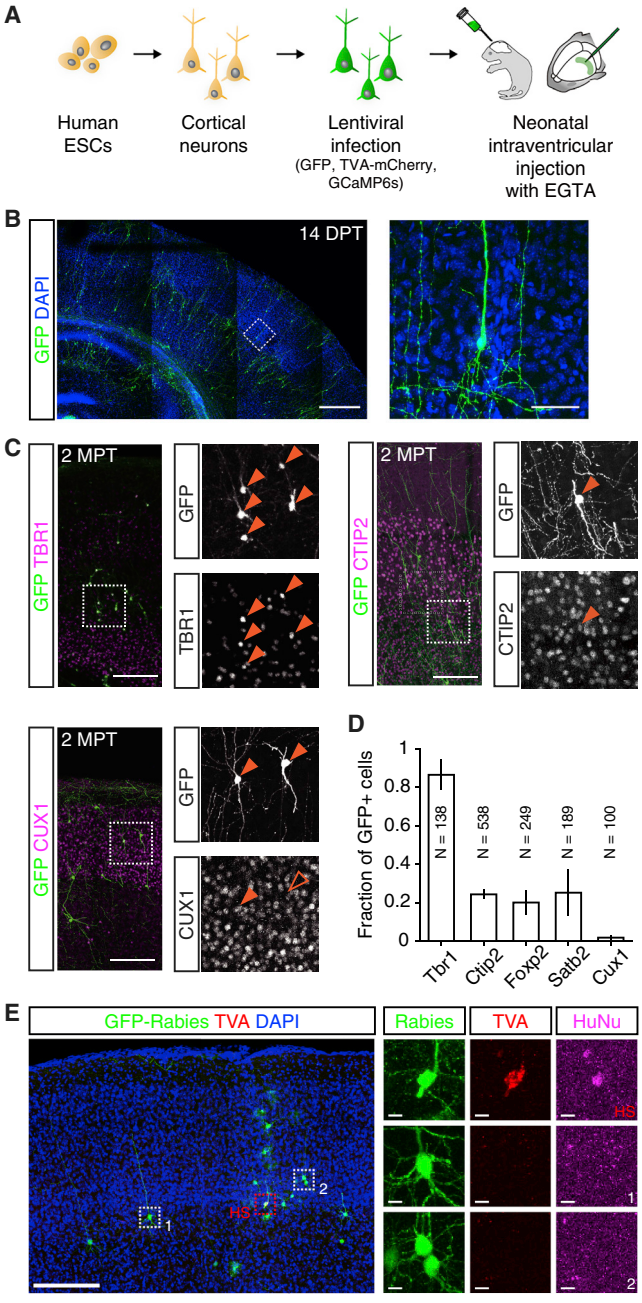

Figure 1. Transplanted Human PSC-Derived Cortical Neurons Integrate as Single Cells in the Mouse Cortex

(A) Human ESC differentiation and transplantation protocol.

(B) Left: confocal image of immunostained coronal section from the brain of a transplanted animal showing GFP$^+$ transplanted human neurons (green) integrated in the mouse cortex, 14 days post-transplantation (DPT), with cell bodies stained with DAPI (blue). Right: high magnification of the boxed subregion on the left (dashed lines). Note the radial orientation and extended apical processes of the human cortical neurons.

(C) Example images of cortical sections from transplanted animals immunostained for markers of deep (Tbr1, Ctip2, Foxp2) and upper (Satb2, Cux1) cortical layer identity at 2 months post-transplantation (2 MPT).

(D) Fraction of GFP$^+$ human neurons expressing markers in (C). N denotes the number of sampled human cells for each marker (n = 4 animals).

(E) Monosynaptic rabies virus tracing shows that human neurons make synaptic connections with host mouse cortical neurons at 4 MPT. Left: confocal image of immunostained section of rabies-injected transplanted cortex with starter human cells (HSs) and rabies-labeled presynaptic mouse cortical neurons (1, 2). Right: high magnification of boxed areas on the left (dashed boxes).

Scale bars: (B) left, 500 μm, right, 50 μm; (C) 200 μm; (E) low-magnification image, 200 μm, high-magnification enlargements, 10 μm.

See also Figure S1.

maturation of intrinsic properties, including membrane potential hyperpolarization, decrease in input resistance, increase in maximum sodium currents, and shortening of AP half-width (Figures 2B–2D and S2A–S2E). These changes were paralleled by a decrease in spontaneous activity (Figures 2F and 2G) and increased peak firing rates (Figure 2E). A progressive increase in the rate of incoming spontaneous synaptic events was also seen over the course of several months (Figure 2H), indicating synaptic maturation.

Thus, transplanted human neurons integrating the mouse cortex display protracted physiological maturation over months, until 11 MPT, at which stage their properties resemble those of adult cortical neurons (Beaulieu-Laroche et al., 2018; Testa-Silva et al., 2014). This is in stark contrast to mouse neurons transplanted in the mouse cortex, which mature in only a few weeks as the host cortical neurons (Falkner et al., 2016; Gaspard et al., 2008; Michelsen et al., 2015). This is unlikely to be a consequence of the delayed maturation of the transplanted host cortex, as mouse L5 pyramidal cells in the cortex of transplanted animals were mature at 6 weeks, similar to control untransplanted mice (Figures S2F–S2K). Prolonged maturation was also observed in human neurons obtained using an alternative protocol of *in vitro* corticogenesis (Shi et al., 2012) (Figures S2D and S2E).

We conclude that transplanted human cortical neurons mature according to a consistently protracted schedule that seems independent of the differentiation or transplantation methods.

The functional maturation of neurons is coordinated with their morphogenesis. To explore this important aspect, a subset of the recorded neurons (n = 28) were filled with biocytin and their morphologies digitally reconstructed and analyzed. We observed over time (1–7 MPT) pronounced changes of dendritic length and complexity (Figures 3A–3C and S3A–S3C), as well as dendritic spine density and morphology (Figures 3D–3F). The transplanted neurons displayed a prolonged timeline of morphogenesis, corresponding to late fetal neurons (Huttenlocher, 1979; Huttenlocher et al., 1982, 1982–1983; Mrzljak et al., 1990; Petanjek et al., 2011), which was strongly correlated with functional maturation parameters (Figures 3G and 3H).

Human cortical pyramidal neurons are characterized by high spine density and large spine size compared to mouse neurons (Benavides-Piccione et al., 2002). At 10 MPT, xenotransplanted human neurons showed lower spine density than adult mouse L5 neurons (Figure S3D), which is indicative of incomplete maturation in line with the human *in vivo* timeline (Huttenlocher et al., 1982–1983; Petanjek et al., 2011; Rakic et al., 1986).

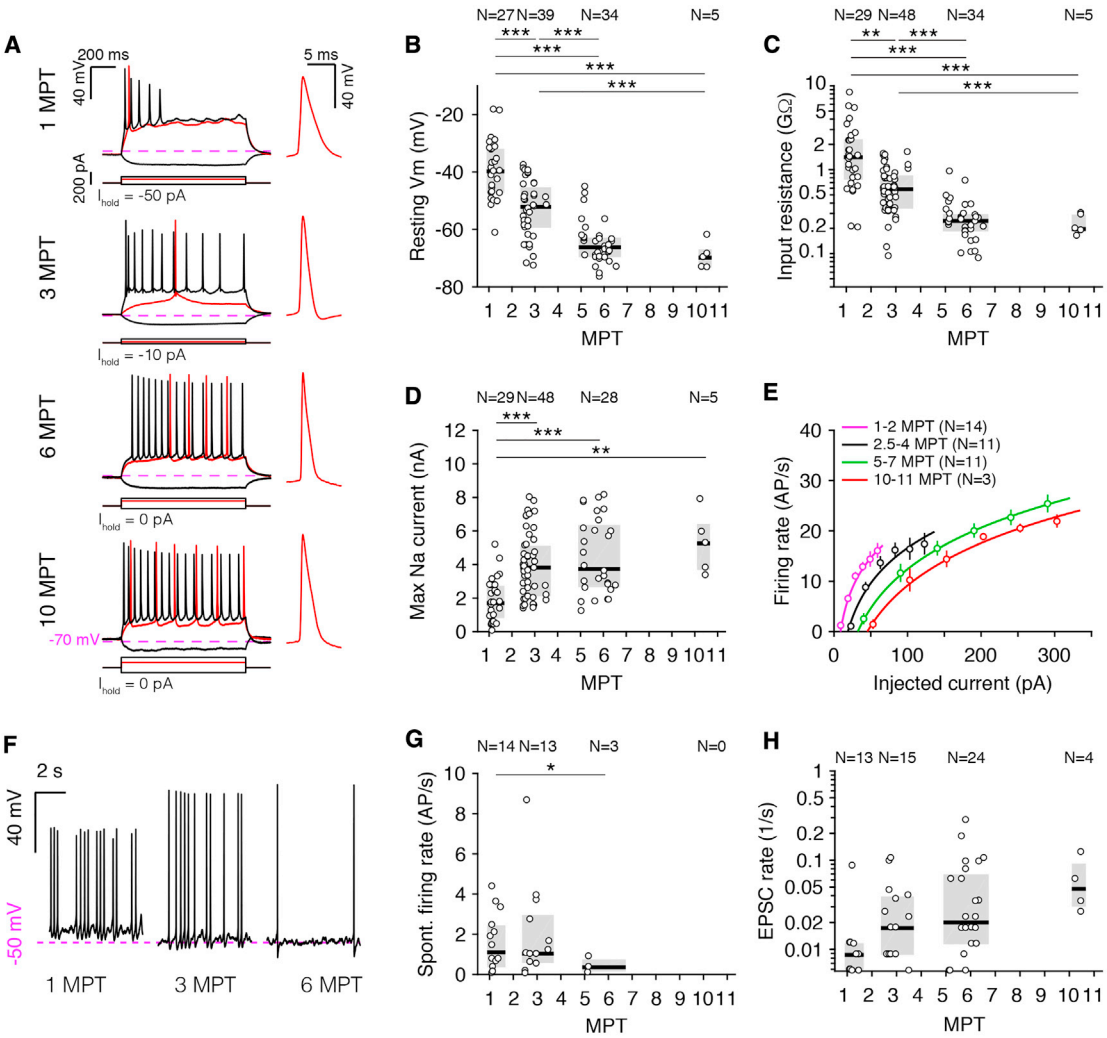

Figure 2. Xenotransplanted Human Cortical Neurons Show Prolonged Maturation

(A) Whole-cell patch-clamp recordings in acute brain slices of xenotransplanted human neurons from 1 to 11 MPT. Left: representative membrane potential responses to hyperpolarizing (black) and depolarizing (red and black) current steps recorded at 1, 3, 6, and 10 MPT. Right: first action potential (AP) to minimal (rheobase) current injection. The offset current (I_{hold}) was adjusted, so the membrane potential was approximately −70 mV (dashed lines). AP shape and spiking response mature progressively.

(B–D) Resting membrane potential (B), input resistance (C), and maximum sodium current (D) of xenotransplanted neurons versus time elapsed since transplantation. N denotes number of cells.

(E) Firing rate versus input current (F-I) curves of cells grouped by time elapsed since transplantation. The markers and error bars indicate means ± SEMs for each group. The continuous lines are power-law fits (see Method Details). Note the rightward shifts of the F-I curves with maturation.

(F) Example recordings of spontaneous activity (I_{hold} = 0 pA) at 1, 3, and 6 MPT. Note the progressive hyperpolarization and reduction of spontaneous firing.

(G) Spontaneous firing rates versus time elapsed since transplantation. No cells showing spontaneous firing were observed after 6 MPT.

(H) Rate of spontaneous incoming excitatory post-synaptic currents versus time elapsed since transplantation.

The pooled data in (B)–(D), (G), and (H) are represented as medians and interquartile ranges. *$p < 0.05$; **$p < 0.01$; and ***$p < 0.001$; Welch's one-way ANOVA with Games-Howell post hoc pairwise comparisons.

See also Figure S2.

Spine sizes and neck lengths of xenotransplanted neurons were higher than those of host mouse neurons (Figures 3I–3K) and in the range of those reported in the human cortex (Benavides-Piccione et al., 2002). This suggests that species-specific features of human neurons—for example, greater spine size—could be acquired by xenotransplanted cells.

These data indicate that transplanted human cortical neurons integrated as single cells in the mouse cortex follow a coordinated program of functional and morphological maturation that is similar to the one observed in the human cortex *in vivo*, which is distinct from the much faster-developing mouse cortical tissue.

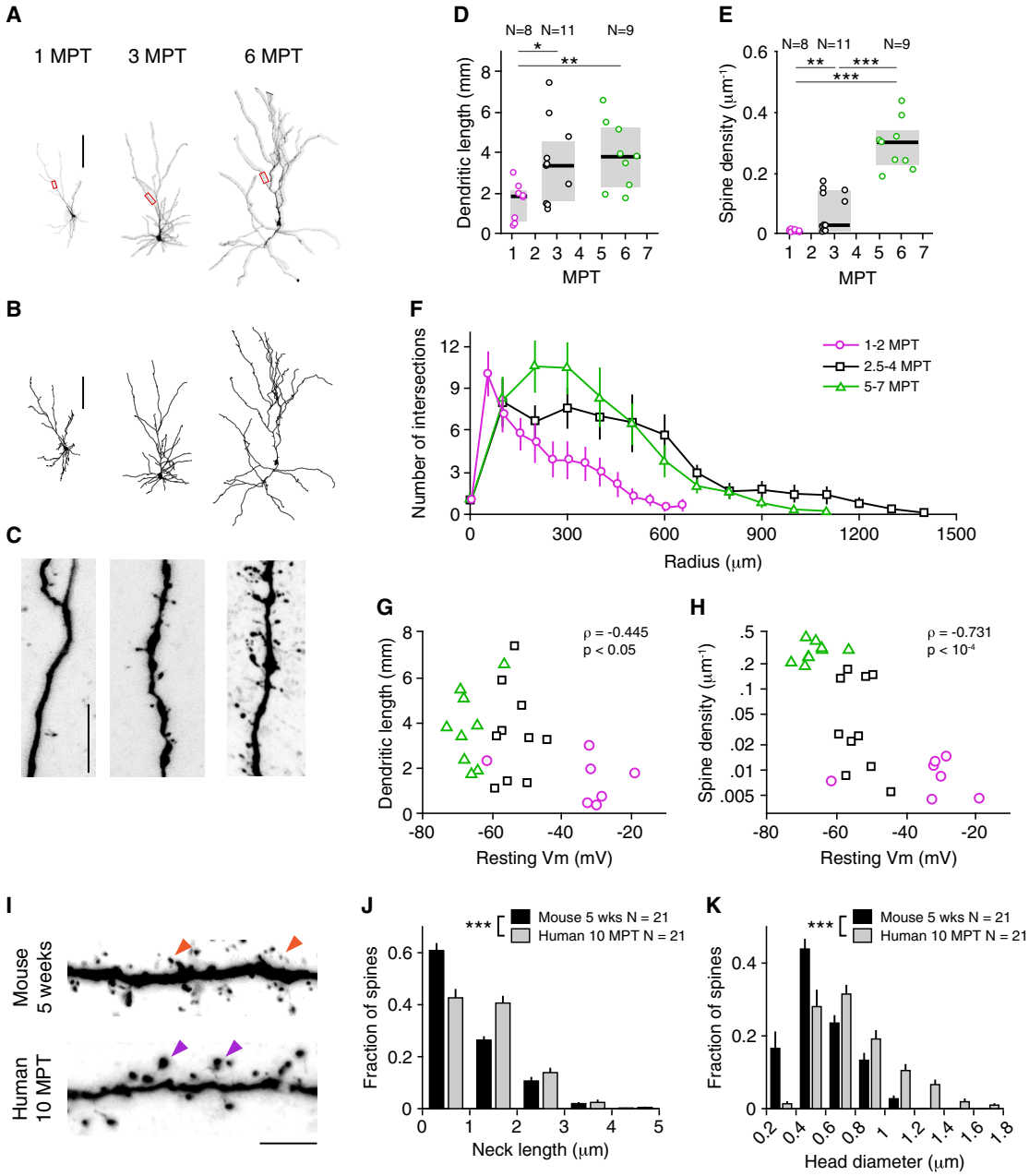

Figure 3. Morphological Maturation of Xenotransplanted Human Cortical Neurons over Months

(A) Confocal images of representative biocytin-filled neurons at 1, 3, and 6 MPT. The boxed areas are shown enlarged in (C).

(B) Three-dimensional reconstructions of the cells shown in (A).

(C) High-magnification confocal images of the dendritic branches highlighted in red in (A). Note the appearance of spines at ~3 MPT and the significant increase in spine density at ~5 MPT.

(D and E) Development of dendritic length (D) and spine density (E) for 28 reconstructed cells. Notice the marked separation in (E) between cells before 4 MPT and after 5 MPT.

(F) Sholl analysis for the reconstructed cells, segregated in three groups according to their age.

(G and H) Dendritic length (G) and spine density (H) as a function of resting membrane potential (Vm). Each marker represents a cell: magenta circles are cells aged 1–2 MPT, black squares are cells aged 2.5–4 MPT, and green triangles are cells aged 5–7 MPT.

(I–K) Comparison of dendritic spine morphology between mouse cortical neurons at 5 weeks of age and human transplanted neurons at 10 MPT. (I) High-magnification images of mouse (top) and human (bottom) dendritic branches. Orange (purple) arrowheads indicate small- (large-)head dendritic spines. (J and K) Distributions of neck lengths (J) and head diameters (K) for human and mouse dendritic spines.

(legend continued on next page)

Transplanted Human Neurons Display Juvenile-like Dendritic Spine Structural Dynamics in Adult Mouse Cortex

As transplanted human neurons develop according to a prolonged timeline, they appear to retain juvenile properties in an otherwise mature mouse brain. A critical feature of juvenile neurons is their structural dynamics, which precedes the establishment of synaptic connectivity (Grutzendler et al., 2002; Zuo et al., 2005). To assess the dynamics of synaptic maturation and cellular integration of transplanted neurons, we performed chronic longitudinal cellular imaging of their dendritic spines *in vivo* (Figure 4; Video S1). Xenotransplanted animals (n = 5) were imaged using a two-photon microscope through a chronically implanted glass window positioned over the occipital cortex (Figure 4A). The GFP-labeled cells were located using a combination of widefield imaging and 2-photon microscopy (Holtmaat et al., 2006; Trachtenberg et al., 2002; Zuo et al., 2005), and the same cells and dendrites were imaged at 2-week intervals for periods up to 12 weeks, focusing on groups of mice that were 3 or 7 MPT at the start of time-lapse imaging (Figures 4B and 4C).

These experiments revealed that in our xenotransplantation assay, human cortical neurons show increasingly stable dendritic spine dynamics, comparable to juvenile mouse cortical neurons (Cruz-Martín et al., 2010; Falkner et al., 2016). Consistent with *ex vivo* data (Figure 3F), xenotransplanted human cortical neurons showed an increase in spine density up to 10–12 MPT (Figure 4D; Table S1), reaching values similar to those reported for human neurons at 1–2 years of age (Jacobs et al., 1997, 2001; Petanjek et al., 2011).

The spine turnover ratio, a measure of cortical dynamics and plasticity (Holtmaat et al., 2005), was still quite high at 3–6 MPT, reflecting juvenile properties of the neurons. It then decreased at 7–10 MPT, indicating that the neurons had reached a more stable stage (Figure 4E), although still more unstable than the adult mouse cortex (Grutzendler et al., 2002; Zuo et al., 2005). This change in spine turnover ratio was accompanied by a pronounced reduction in the number of gained and lost spines (Figure 4F; Table S1). By following spines across multiple consecutive imaging sessions, we observed a flattening of the spine survival function (Figure 4G), reflecting an increase in spine survival rates from ~2 weeks at 3–6 MPT to ~8 weeks at 7–11 MPT (Table S1).

These data support the notion that dendritic spines of transplanted human neurons follow a prolonged timeline that resembles the maturation time of human cortical neurons (Petanjek et al., 2011) and that is largely intrinsic to these neurons, as they still display juvenile-like dynamic patterns at 3–6 MPT (e.g., in a mature mouse brain environment) (Falkner et al., 2016; Holtmaat et al., 2005; Tjia et al., 2017; Zuo et al., 2005). Critically, the stabilization of the dendritic spines at later stages supports the view that neurons progressively integrate synaptically within the host brain, despite their extended maturation.

Transplanted Human Neurons Display Long-Term Synaptic Potentiation

The observation of structural dynamics, together with an increase in the rate of incoming spontaneous synaptic events (Figure 2H), raised the possibility that transplanted human neurons may display synaptic plasticity. To assess this, we applied a long-term potentiation (LTP) protocol (Nevian and Sakmann, 2006) to xenotransplanted neurons in an *ex vivo* preparation (Figure 5A). We found that human cells aged 3–6 MPT displayed response potentiation, measured as the amplitude of the excitatory post-synaptic potential (EPSP), lasting for >30 min after the application of the pairing stimulus (Figure 5B). At the population level, we found that approximately two-thirds of the tested human neurons displayed LTP (n = 7/10; Figures 5C and 5D). Analogous experiments in mouse L5 pyramidal cells of 3-month-old mice also revealed LTP, although with a smaller magnitude of the response increase (Figure 5E). These results indicate that xenotransplanted human cortical neurons present robust functional synaptic plasticity comparable to host cortical pyramidal neurons.

Transplanted Human Neurons in the Visual Cortex Display Sparse Tuned Activity Resembling the Activity of Host Cortical Neurons

Synaptic integration within the host cortex may allow xenotransplanted neurons to respond to internal and external events and encode information. To assess synaptic integration functionally *in vivo*, we performed cellular calcium imaging in response to sensory stimulation (Figure 6). We imaged in the visual cortex the spontaneous and sensory-evoked responses of human neurons expressing both the calcium indicator GCaMP6s and the nuclear label nls-dTomato (Figures 6A and S1). GCaMP6s expression was induced by doxycyclin. At 5–9 MPT, transplanted neurons in L2/3 (100–300 μm) were targeted using the nuclear label as the landmark. Visual stimulation was achieved by presenting drifting grating stimuli or prolonged epochs of equiluminant gray screen to the contralateral visual field (Figure 6B).

These experiments revealed robust spontaneous and visually driven activity in more than one-fourth of the sampled xenotransplanted cells, with more than two-thirds of spontaneously active cells displaying responses to visual stimulation (Figures 6C–6J; Video S2). We characterized a total of 155 human neurons measured from 5 animals (54 sessions for visual stimulation, 15 sessions for spontaneous activity). In the absence of visual contrast (gray screen, experiment expt. A), ~32% of identified cells showed significant activity (>0.5 transients/min, 25 of 77 labeled neurons; Table S1). During stimulation with grating stimuli, a slightly higher fraction, ~35%, of cells showed calcium activity (55 of 155 labeled neurons, expt. B). Among the cells showing calcium activity, visual stimulation increased calcium

Scale bars: (A) and (B) 100 μm, (C) 10 μm, and (I) 5 μm. Markers and error bars indicate means ± SEMs. In (D) and (E), pooled data are represented as medians and interquartile ranges. *$p < 0.05$; **$p < 0.01$; and ***$p < 0.001$. (D) and (E) Welch's one-way ANOVA with Games-Howell post hoc pairwise comparisons; (J) and (K) Kolmogorov-Smirnov test. In (G) and (H), the reported value of ρ is Spearman's rank correlation coefficient.
See also Figure S3.

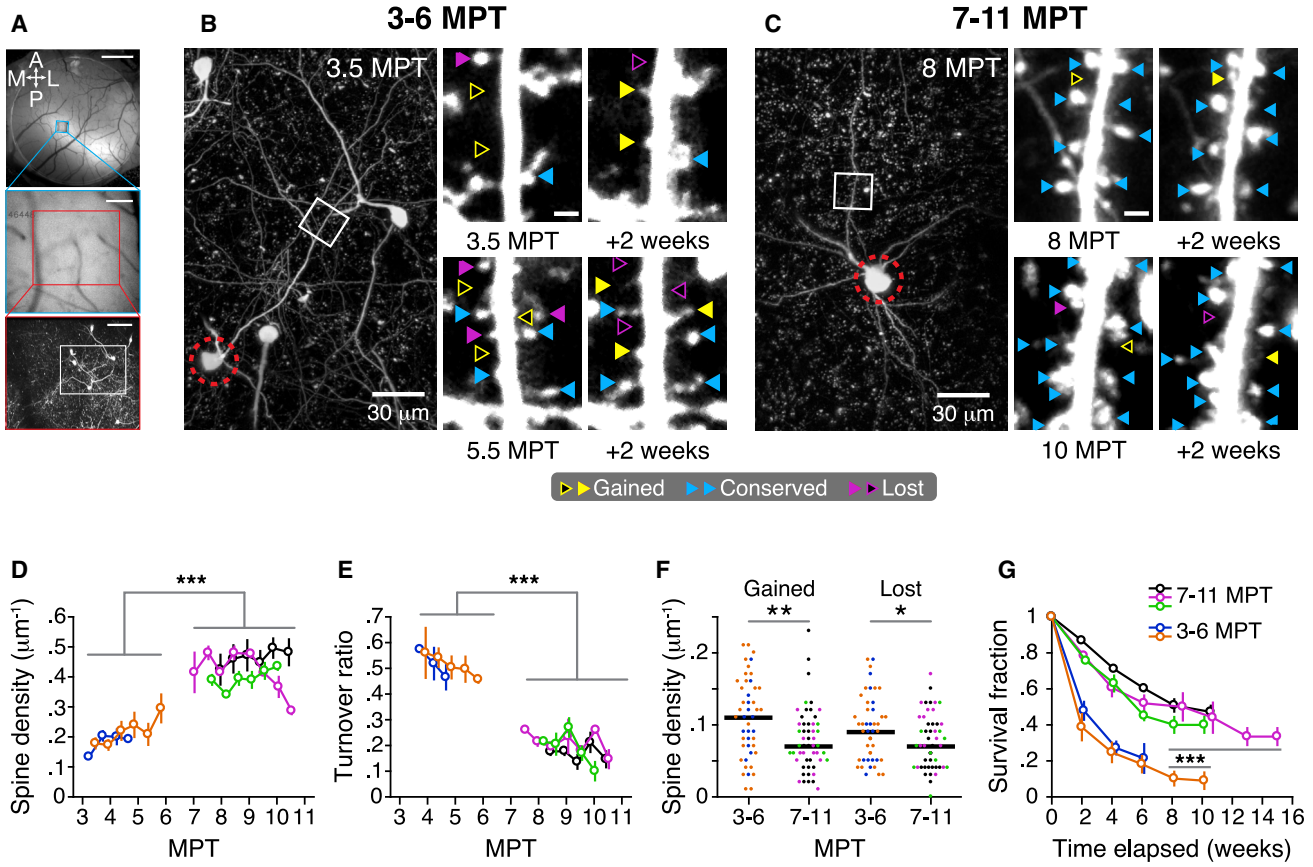

Figure 4. Transplanted Human Cortical Neurons Develop Increasingly Stable Dendritic Spines Structural Dynamics

(A) Cellular imaging of xenotransplanted cells, dendrites, and spines over weeks. A cranial window was implanted and GFP-labeled transplanted cells in superficial layers of the cortex (100–250 μm) were imaged using a 2-photon microscope at 1- to 2-week intervals for up to 15 weeks starting at 3 MPT (n = 2 animals) or 7 MPT (n = 3 animals). Surface blood vessels and two-photon images were used to target neurons and dendrites across weeks. Top: camera view of the cranial window with 2× lens and blue/green excitation/collection. Center: camera view of targeted region through the 25× multiphoton objective lens. Bottom: maximum intensity projection of a two-photon image stack centered on a cluster of human neurons. Scale bars: 1 mm (top), 200 μm (center), and 100 μm (bottom).

(B) Example of dendritic spines dynamics at 3–6 MPT for neuron cluster in (A). Left: maximum intensity projection image showing cell soma (red dashed circle) and a targeted dendritic branch segment (white box). Right: spine annotation of dendritic segment shown on the left at 3.5 and 5.5 MPT (white box, left column) and 14 days later (right column), showing spine gain (yellow), spine loss (purple), and conserved spines (blue).

(C) Example of dendritic spine dynamics at 7–10 MPT. The conventions are as in (B). Note the increase in conserved spines (blue) relative to spine gains and losses (yellow and purple).

(D) Spine density as a function of time elapsed since transplantation for five animals. Each set of colored symbols summarizes the data of 2–7 targeted dendritic branches from 1 animal. Spine density at 7–10 MPT is significantly higher than at 3–6 MPT (n = 3 versus n = 2 animals, 1-way mixed ANOVA). Note the trend of increasing spine density with elapsed time at 3–6 MPT. Error bars denote SEMs across branches.

(E) Spine turnover ratio as a function of elapsed time. Turnover ratio at 7–10 MPT is significantly lower than at 3–6 MPT (n = 3 versus n = 2 animals, 1-way mixed ANOVA).

(F) Density of gained and lost spines at 3–6 MPT and 7–10 MPT. Each data point corresponds to one dendritic segment at one time point. Note the significant decreases in the densities of gained and lost spines between 3–6 MPT and 7–10 MPT (n = 2 versus n = 3 animals, 1-way ANOVA).

(G) Fraction of conserved spines (survival fraction) as a function of elapsed time. Note how the survival fraction measured at 7–10 MPT decays more slowly than at 3–6 MPT (n = 3 versus n = 2 animals, 1-way mixed ANOVA). Markers and error bars indicate means ± SEMs.

*p < 0.05; **p < 0.01; and ***p < 0.001.

transients rates (Figure 6H; Table S1) and amplitudes (Figure 6I; Table S1). These findings were confirmed for matched populations (Figures S4C and S4D). Thus, transplanted neurons not only fire spontaneously but also receive sensory inputs from host neurons, which could be from neighboring cortical neurons or from thalamic neurons.

Notably, the activity of xenotransplanted neurons was highly decorrelated (Figures 6D, 6J, S4E, and S4F). Xenotransplanted neurons fired independently, with cells showing calcium transients at distinct time points (Figure 6D). Accordingly, calcium activity time courses in the presence and absence of visual stimulation were only weakly correlated (Table S1). This suggests

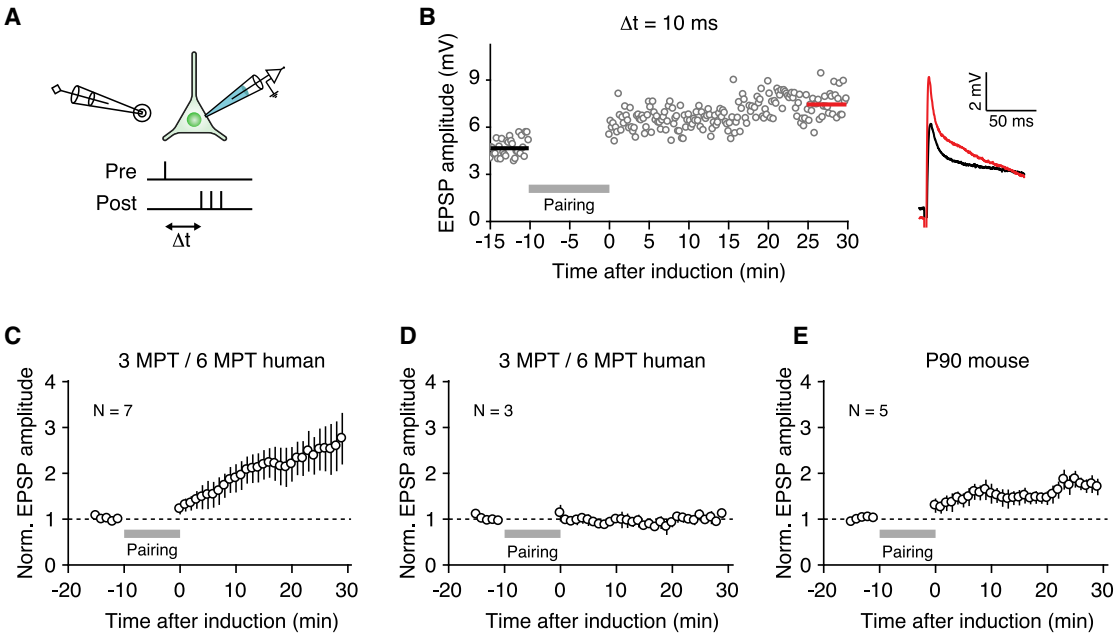

Figure 5. Transplanted Human Cortical Neurons Show Long-Term Potentiation of Local Cortical Inputs

(A) Schematic of paired stimulation long-term potentiation (LTP) induction paradigm.

(B) Example of one representative cell that showed potentiation.

(C) EPSP amplitude as a function of time in response to 10 min of pre- to post-pairing for the n = 7 human cells that displayed LTP.

(D) Same as (C), but for the n = 3 human cells that displayed a stable EPSP amplitude in response to the pairing protocol.

(E) Same as (C) and (D), but for n = 5 mouse cells recorded in 3-month-old mice.

Markers and error bars indicate means ± SEMs.

that xenotransplanted neurons receive highly specific inputs, both from the eyes and other sources.

To examine the specificity of these inputs, we examined the tuning of responses for grating direction and orientation (Figure 7). Neurons in mouse visual cortex are characterized by diversely tuned responses to specific properties of visual stimuli (e.g., stimulus orientation stimulus direction) (Niell and Stryker, 2008). If human neurons receive inputs from host neurons, then they should also show such diversely tuned responses to visual stimuli.

Approximately 25% of xenotransplanted neurons (38 of 155 labeled neurons) showed clear visual responses (median $\Delta F/F_0$ response >3 SDs over baseline for >1 s), resulting in 69% (38 of 55) of neurons that showed calcium activity being deemed visually responsive. Responses were diversely tuned for different directions of motion and spatial orientations (Figure 7A). To quantify these response properties, we computed the stimulus direction and orientation eliciting the strongest response (preferred direction and orientation) and indices quantifying the selectivity of responses (direction selectivity index [DSI] and orientation selectivity index [OSI]). We compared these data to those obtained from mouse L2/3 pyramidal neurons (4,260 cells, n = 1 animal, mouse line: CaMKII-tTA × TRE-GCaMP6 line G6s2), as well as from host neurons recorded in transplanted animals (191 cells, n = 2 animals). Responses from mouse cortical neurons in control and transplanted animals were similar, indicating no overt disruption of host circuitry by the transplantation and by the presence of human neurons in the brain (Figure S5).

Consistent with the weak activity correlations observed between cell pairs, xenotransplanted neurons showed diversely tuned responses (median OSI = 0.36 and DSI = 0.25; Figures 7B, 7D, and 7F), with tuning properties resembling those of mouse neurons in control animals (Figures 7C, 7E, 7G, and S5A–S5C) and in transplanted animals (Figures S5D–S5F). Orientation and direction selectivity were pronounced, with 60% and 78% of visually responsive cells showing tuned responses for stimulus orientation and direction (OSI and DSI >0.2; Figures 7B and 7F), similar to mouse neurons (Table S1). Compared to mouse neurons, visually responsive human neurons showed weaker selectivity for orientation but not for direction of motion (Table S1), which may reflect the maturing nature of the underlying circuitry (Rochefort et al., 2011).

These findings indicate that xenotransplanted human neurons successfully integrate and inherit functions of the host cortical neurons, including tuned responses to sensory stimuli.

DISCUSSION

The mechanisms underlying the development of human neurons and synapses have major implications for brain evolution, function, and disease. While *in vitro* PSC-based models hold great promise to study human neural development (Astick and Vanderhaeghen, 2018; Di Lullo and Kriegstein, 2017; Lancaster

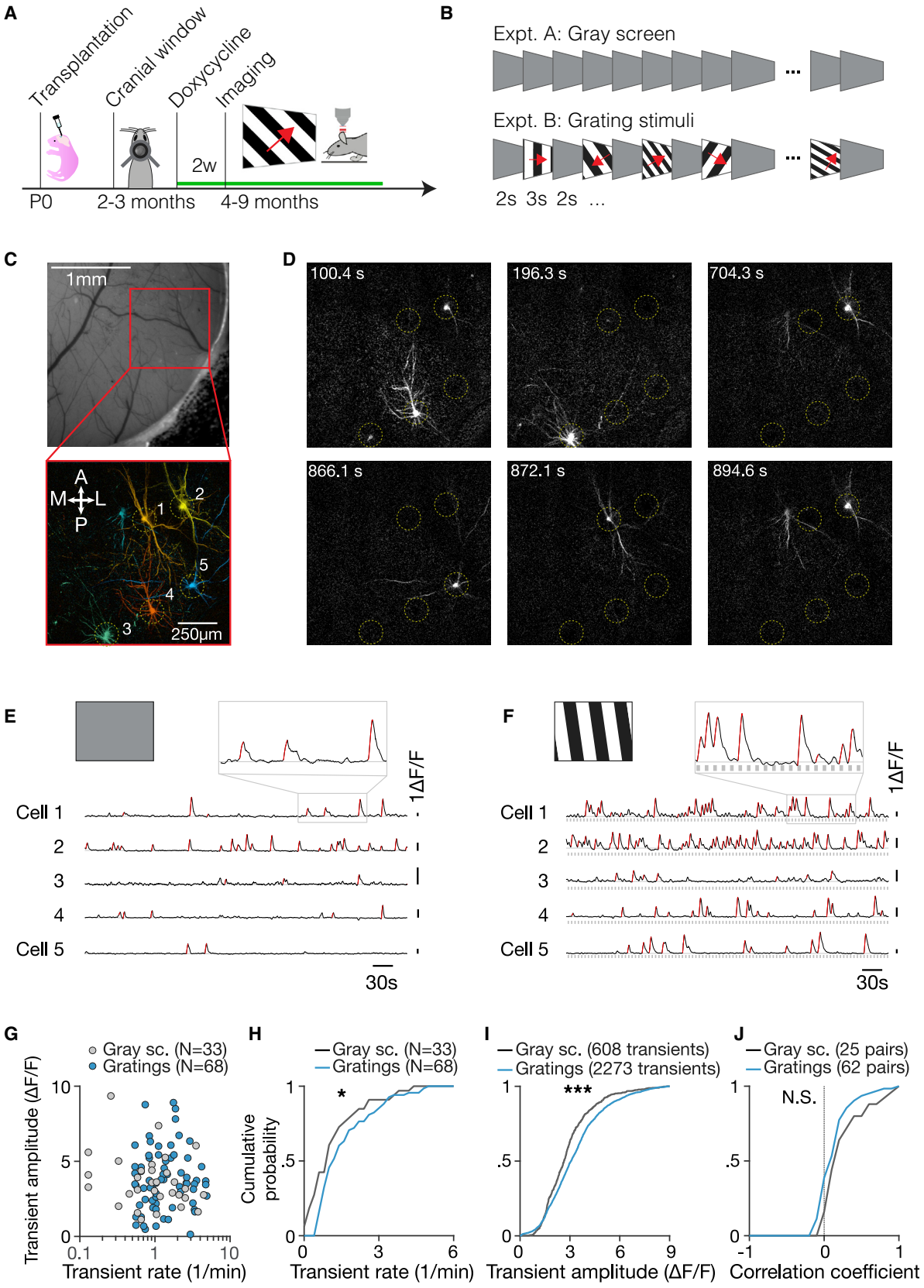

(legend on next page)

and Knoblich, 2014), their use in studying neuronal function in the context of a physiologically relevant circuit has remained difficult, whether using monoadherent cultures, organoids, or xenotransplantation.

In contrast, here, we find that when human neurons can integrate as single cells within mouse cortical circuits, they display strong connectivity with the host neurons. This model robustly recapitulates key milestones of human neuronal development not reported so far using xenotransplantation or *in vitro* models. Specifically, the transplanted neurons displayed (1) coordinated morphological and physiological maturation at the single-cell level, (2) robust dendritic spine dynamics followed by stabilization and synaptogenesis, (3) functional synaptic plasticity, and (4) physiological responses to sensory stimulation that are similar to those of native cortical neurons.

We and others previously reported a prolonged timeline of morphological development for transplanted human cortical neurons that was proposed to be in line with human cortical neoteny (Anderson and Vanderhaeghen, 2014; Espuny-Camacho et al., 2013; Maroof et al., 2013; Nicholas et al., 2013). However, the temporal pattern of synaptic maturation and functional integration of xenotransplanted human cortical neurons had not been characterized systematically. Moreover, it had remained unclear whether the prolonged synaptic maturation of human neurons xenotransplanted in the mouse cortex is genuinely intrinsic to these cells or a property of transplanted cells remaining mostly isolated from the rest of the brain. Here, we find that xenotransplanted neurons integrated as single cells within the mouse cortex develop morphologically and functionally following a months-long timeline that is remarkably similar to the one reported in the human developing brain (Defelipe, 2011; Sousa et al., 2017). Moreover, human neurons are initially as highly dynamic as juvenile neurons and then become progressively more stable, albeit only over a prolonged 6- to 11-month-long period. In contrast, dendritic spines of mouse neocortical neurons display high dynamics and turnover only for a few weeks before adulthood (Hofer et al., 2009; Holtmaat and Svoboda, 2009). Our observation that dendritic spines on human neurons display highly dynamic patterns in the adult mouse cortex provides strong evidence that the prolonged development of human cortical neurons is not likely to be an experimental artifact, but rather an inherent biological feature of human neurons. The intrinsic retention of juvenile properties in human cortical neurons may constitute the cellular basis of the brain neoteny that is thought to have played a major role in human evolution (Gould, 1992). That said, it remains possible that a part of the prolonged pattern observed here also reflects the fact that xenotransplantation provides only a suboptimal environment for the development of the transplanted cells. However, it is interesting to note in this context that recent work has shown faster development of chimpanzee versus human neurons xenotransplanted in the mouse brain (Marchetto et al., 2019).

Our model thus constitutes a promising experimental system to elucidate the mechanisms controlling the timeline of neuronal maturation, in particular by studying in transplanted neurons the function of genes potentially involved in human neuronal neoteny (Charrier et al., 2012; Suzuki et al., 2018).

The plasticity displayed by juvenile human neurons in the adult mouse brain also raises the fascinating possibility of their potential influence on the plasticity of the host cortical circuits, by analogy with the known effects of transplanted embryonic interneurons on cortical plasticity (Southwell et al., 2014).

Despite their prolonged development, the transplanted neurons are not stalled in an immature state. Instead, they gradually display increased spine density and stability, as in normal development, to finally reach levels that are close to

Figure 6. Transplanted Human Cortical Neurons Show Decorrelated Spontaneous and Visually Evoked Activity

(A) Assay for *in vivo* calcium imaging of transplanted human neurons in the mouse cortex. Xenotransplanted neurons were engineered to express doxycycline-inducible GCaMP6s and nuclear label dTomato. A chronic cranial window was implanted at 2–3 MPT over left visual cortex, and starting at 4.5 MPT, animals were head fixed awake under a 2-photon microscope with a display monitor facing the right eye. Somatic calcium signals were recorded from xenotransplanted neurons in superficial (100–300 μm) layers.

(B) Neurons were stimulated with static gray screen (expt. A) or square-wave drifting gratings of different temporal frequencies, spatial frequencies, spatial orientations, and directions of motion (expt. B).

(C) Widefield fluorescence camera image (top) and two-photon field of view showing imaged cell bodies and proximal dendrites (bottom). Images generated using activity correlation analysis (see also Figures S4E and S4F).

(D) Differential delta fluorescence (ΔF) images showing human neurons firing at a distinct time points during the drifting gratings experiment. Yellow dashed circles mark the location of five neurons showing activity during the experiment.

(E) Spontaneous activity of human neurons in the visual cortex shown in (C) and (D). Somatic calcium time courses of simultaneously imaged neurons (black lines) in the absence of visual stimulation (static gray screen, expt. A) with identified calcium transients highlighted (red) are shown. Calcium transients are defined as epochs where the calcium signal increase per second exceeds 2 × SD of the distribution (STD) of baseline.

(F) Same as (E), for the visual stimulation experiment (expt. B). Somatic calcium time courses of simultaneously imaged neurons during the presentation of grating stimuli (expt. B, gray squares) for the same five neurons in (C) and (D) are shown. Note how visual stimulation increases the frequency and amplitude of calcium transients (red lines).

(G) Scatter plot of calcium transient rate versus amplitude for all spontaneously active human neurons (33 cells from 5 animals, gray dots) and for visually responsive neurons (68 cells from 6 animals, blue dots). Visually responsive neurons are defined as having a median $\Delta F/F_0$ response >3 SD over baseline for >1 s.

(H) Cumulative plots show distributions of transient rates for gray screen (gray line, n = 33 neurons) and visual stimulation (blue line, n = 68 neurons).

(I) Same as (H), for transient amplitude.

(J) Cumulative plots show distributions of activity correlations computed between calcium activity time courses of simultaneously recorded pairs for gray screen (gray line, n = 25 pairs) and visual stimulation data (blue line, n = 62 pairs). The calcium activity of human neurons is only weakly correlated across cell pairs, in the presence and absence of visual stimuli, indicating that they respond to distinct inputs.

See also Figure S4.

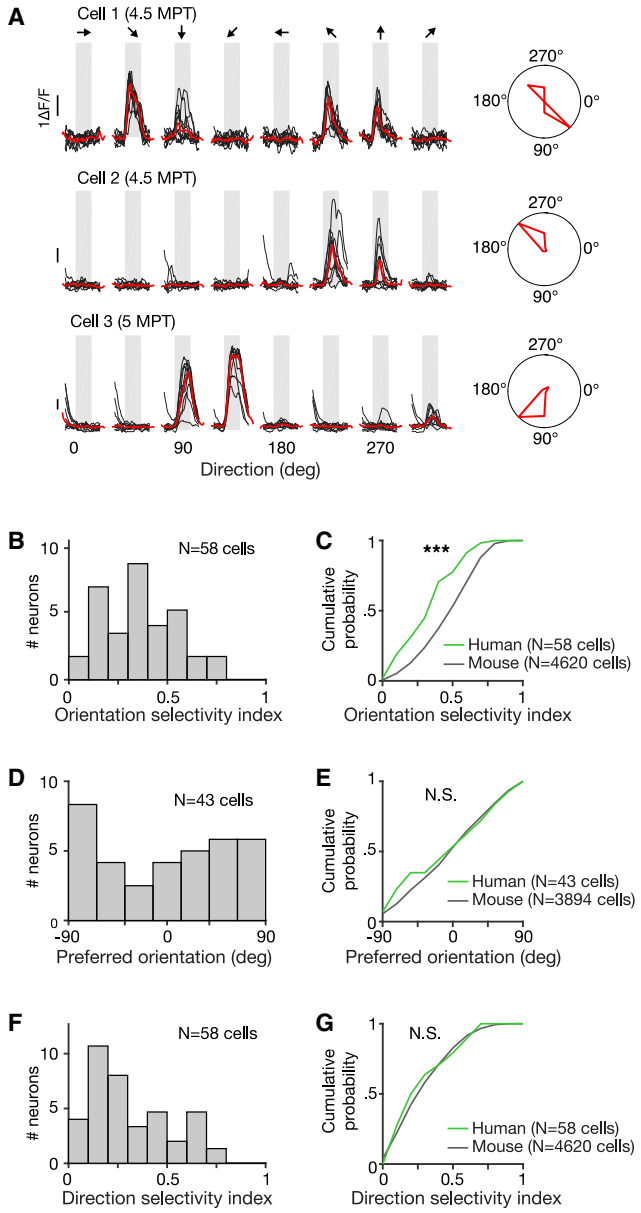

Figure 7. Transplanted Human Neurons Show Orientation and Direction Tuned Responses Resembling the Responses of Mouse Visual Cortical Neurons

(A) Single-trial (black) and median (red) somatic calcium time courses of three human neurons aligned to visual stimulation epoch (gray). The responses shown are for grating stimuli of eight different directions of motion (left or right), together with corresponding median response polar plots.

(B) Distributions of orientation selectivity indices computed from calcium time courses of human neurons.

(C) Cumulative plots comparing the distributions of orientation selectivity indices of human (green line) and mouse (black line) cortical neurons. Lower orientation selectivity values are consistent with the maturing state of the human neurons.

(D) Distributions of preferred orientations computed from calcium time courses of human neurons.

(E) Cumulative plots comparing the distributions of preferred orientations of human (green line) and mouse (black line) cortical neurons.

(F) Distributions of direction selectivity indices computed from calcium time courses of human neurons.

(G) Cumulative plots comparing the distributions of direction selectivity indices of human (green line) and mouse (black line) cortical neurons. The distributions of preferred orientations and direction selectivity indices of human and mouse neurons were similar. Mouse neural recordings are from transgenic mouse V1 L2/3 pyramidal neurons (mouse line CaMKII-tTA x TRE-GCamp6.lineG6s2). See also Figure S5.

those of mouse adult neurons. This contrasts with recent findings in PSC-derived human cortical neurons transplanted as bulk cell populations, which displayed rapid dendritic spine turnover throughout the experiment (spine half-life <4 days versus 2 weeks at 3–4 months), and reached very limited levels of synaptic connectivity with the host brain (Real et al., 2018). These differences illustrate how the transplantation paradigm, and in particular whether transplanted neurons integrate as single cells, is a key determining factor on the final levels of maturation and connectivity that can be achieved by the transplanted neurons. The xenotransplanted neurons also reach much more advanced stages of spine maturation than reported so far in *in vitro* models of human corticogenesis, using adherent cultures or organoids (Astick and Vanderhaeghen, 2018; Di Lullo and Kriegstein, 2017; Lancaster and Knoblich, 2014), suggesting that the host brain provides not only a permissive environment but also instructive cues for spine morphogenesis and synaptogenesis.

The transplanted neurons also display robust functional synaptic plasticity in the form of long-term potentiation. As this is a major readout of synaptic function within a whole circuit, this provides a unique opportunity to model human neuronal plasticity in health and disease (Cruz-Martín et al., 2010; Ebert and Greenberg, 2013; Murmu et al., 2013; Spires-Jones and Hyman, 2014; Zoghbi and Bear, 2012).

While the xenotransplanted human neurons described here have achieved unprecedented maturation, some of their properties still correspond to a less mature stage than adult human neurons. For instance, morphologically, the transplanted human neurons display smaller cell bodies and dendritic arbors than adult human cortical neurons, and functionally only a fraction of the neurons display visual responses, in line with the fact that human cortical neurons take up to several years to reach full maturity. Similarly, dendritic spine dynamics suggest that neurons are still undergoing synaptic growth and have not yet reached the stage of dendritic spine/synapse pruning, which is supposed to last for more than a decade in some cortical areas (Petanjek et al., 2011). However, the transplanted neurons at the latest examined stages display a larger size distribution of dendritic spines, comparable to human cortical neurons *in vivo* (Benavides-Piccione et al., 2002). It will be interesting to test whether transplanted human neurons that are allowed to develop for even longer periods can acquire other species-specific properties of mature human neurons, including a higher capacity of transmitting information (Beaulieu-Laroche et al., 2018; Eyal et al., 2016; Testa-Silva et al., 2014).

Our model provides a first characterization of the function of human neurons in an intact circuit *in vivo*. We report that up to

25% of the xenotransplanted neurons and 69% of those that show calcium transients display functional responses to visual sensory stimulation. These neurons fire in a decorrelated fashion and display visually tuned responses resembling those of mouse cortical neurons (Andermann et al., 2011). This shows that xenotransplanted human neurons can integrate in the adult mouse brain and gain information-processing functioning. This is in contrast with data obtained using neural organoids in vitro or following transplantation (Mansour et al., 2018; Trujillo et al., 2019), which show highly correlated activity indicative of circuit immaturity. Our data also constitute a striking example of the capacity of single neurons to adapt to the dominant influence of the circuit in which they are integrated. That said, while the recorded responses are remarkably similar to those of host neurons, it is important to note that the fraction of cells that display these responses remains a 25% minority. This could be due in part to the connectivity of the cells that may be still too low, as their spine density remains lower than adult (mouse or human) values, even at 10 MPT, which, again, could reflect their neotenic development, but also an excitatory/inhibitory imbalance or improper connectivity. Future studies should determine which host presynaptic partners (thalamic or cortical) enable the generation of human neuronal responses, but they should also focus on the acquisition and tuning of sensory responses and determine whether and how they compare to those of host neurons (Mizuno et al., 2018; Rochefort et al., 2011).

Another important implication of our *in vivo* imaging dataset is that genuine functional integration of the transplanted neurons was observed mainly at an advanced adult stage (>6 MPT), implying that juvenile neurons could engage functionally into a mature cortical circuit in relatively old animals and yet display responses highly similar to those of the host neurons. This has potentially important implications in the perspective of brain repair by cell therapy strategies (Tabar and Studer, 2014). The transplantation of human PSC-derived cortical pyramidal neurons into the lesioned adult cortex has been shown to be promising (Espuny-Camacho et al., 2018; Tornero et al., 2013, 2017), but it remains to be tested whether and how transplanted neurons can integrate into damaged circuits up to the functional level shown here following neonatal transplantation, as a key step toward the restoration of damaged brain circuits.

STAR★METHODS

Detailed methods are provided in the online version of this paper and include the following:

- KEY RESOURCES TABLE
- LEAD CONTACT AND MATERIALS AVAILABILITY
- EXPERIMENTAL MODEL AND SUBJECT DETAILS
  - Animals
- METHOD DETAILS
  - Human ESC differentiation into cortical cells
  - Viral constructs
  - Neonatal transplantation
  - FACS and scRNA-seq of transplanted cells
  - Electrophysiology
  - Rabies virus-based monosynaptic tracing
  - Surgical procedures
  - Widefield calcium imaging
  - Two-photon calcium imaging
  - *In vivo* structural imaging
  - *In vivo* functional imaging
  - Immunofluorescence
- QUANTIFICATION AND STATISTICAL ANALYSIS
  - Electrophysiology
  - *In vivo* spine imaging
  - Calcium imaging
  - Morphology reconstructions and analysis
- DATA AND CODE AVAILABILITY

SUPPLEMENTAL INFORMATION

Supplemental Information can be found online at https://doi.org/10.1016/j.neuron.2019.10.002.

A video abstract is available at https://doi.org/10.1016/j.neuron.2019.10.002#mmc6.

ACKNOWLEDGMENTS

The authors thank members of the Vanderhaeghen lab for helpful discussions and J.-M. Vanderwinden of the ULB Light Microscopy Facility for support with imaging. Some of the images were acquired on a Zeiss LSM 880-Airyscan system (Cell and Tissue Imaging Cluster [CIC]), supported by Hercules AKUL/15/37_GOH1816N and FWO G.0929.15 to Pieter Vanden Berghe, KU Leuven. This work was funded by the Vlaams Instituut voor Biotechnologie (VIB), Neuro-Electronics Research Flanders, the European Research Council (ERC Adv Grant GENDEVOCORTEX), the Fondation ROGER DE SPOELBERCH, the EOS Program SYNET, the Fonds de la Recherche Scientifique/Fonds National de la Recherche Scientifique (FRS/FNRS), the Welbio Program of the Walloon Region, the Biowin iCONE program of the Walloon Region, the AXA Research Fund, the Fondation ULB, the Fondation JED, the KU Leuven Research Council grant C14/19/111, the FWO Research Grant 1237220N (to P.V.), and the KU Leuven Research Council grant C14/16/048 (to V.B.). R.I. was supported by a postdoctoral fellowship of the FRS/FNRS and B.L.-P. was supported by a postdoctoral fellowship of the FWO.

AUTHOR CONTRIBUTIONS

Conceptualization & Methodology, D.L., B.V., R.I., V.B., and P.V.; Investigation, D.L., B.V., A.R., B.A.D., L.B., B.L.-P., A.B., L.D., D.G., R.I., V.B., and P.V.; Formal Analysis, D.L., B.V., R.I., V.B., and P.V.; Key Reagents, K.-K.C.; Writing – Original Draft, D.L., B.V., V.B., and P.V.; Writing – Review & Editing, D.L., B.V., A.R., B.A.D., D.L., D.G., R.I., V.B., and P.V.; Funding Acquisition, P.V.; Resources, V.B. and P.V.; Supervision, V.B. and P.V.

DECLARATION OF INTERESTS

The authors declare no conflicts of interest.

Received: May 2, 2019
Revised: August 12, 2019
Accepted: September 30, 2019
Published: November 21, 2019

REFERENCES

Andermann, M.L., Kerlin, A.M., Roumis, D.K., Glickfeld, L.L., and Reid, R.C. (2011). Functional specialization of mouse higher visual cortical areas. Neuron *72*, 1025–1039.

Anderson, S., and Vanderhaeghen, P. (2014). Cortical neurogenesis from pluripotent stem cells: complexity emerging from simplicity. Curr. Opin. Neurobiol. *27*, 151–157.

Astick, M., and Vanderhaeghen, P. (2018). From Human Pluripotent Stem Cells to Cortical Circuits. Curr. Top. Dev. Biol. *129*, 67–98.

Bae, B.I., Jayaraman, D., and Walsh, C.A. (2015). Genetic changes shaping the human brain. Dev. Cell *32*, 423–434.

Beaulieu-Laroche, L., Toloza, E.H.S., van der Goes, M.S., Lafourcade, M., Barnagian, D., Williams, Z.M., Eskandar, E.N., Frosch, M.P., Cash, S.S., and Harnett, M.T. (2018). Enhanced Dendritic Compartmentalization in Human Cortical Neurons. Cell *175*, 643–651.e14.

Benavides-Piccione, R., Ballesteros-Yáñez, I., DeFelipe, J., and Yuste, R. (2002). Cortical area and species differences in dendritic spine morphology. J. Neurocytol. *31*, 337–346.

Bianchi, S., Stimpson, C.D., Duka, T., Larsen, M.D., Janssen, W.G., Collins, Z., Bauernfeind, A.L., Schapiro, S.J., Baze, W.B., McArthur, M.J., et al. (2013). Synaptogenesis and development of pyramidal neuron dendritic morphology in the chimpanzee neocortex resembles humans. Proc. Natl. Acad. Sci. USA *110* (*Suppl 2*), 10395–10401.

Bufill, E., Agustí, J., and Blesa, R. (2011). Human neoteny revisited: the case of synaptic plasticity. Am. J. Hum. Biol. *23*, 729–739.

Charrier, C., Joshi, K., Coutinho-Budd, J., Kim, J.E., Lambert, N., de Marchena, J., Jin, W.L., Vanderhaeghen, P., Ghosh, A., Sassa, T., and Polleux, F. (2012). Inhibition of SRGAP2 function by its human-specific paralogs induces neoteny during spine maturation. Cell *149*, 923–935.

Cruz-Martín, A., Crespo, M., and Portera-Cailliau, C. (2010). Delayed stabilization of dendritic spines in fragile X mice. J. Neurosci. *30*, 7793–7803.

Cunningham, M., Cho, J.H., Leung, A., Savvidis, G., Ahn, S., Moon, M., Lee, P.K., Han, J.J., Azimi, N., Kim, K.S., et al. (2014). hPSC-derived maturing GABAergic interneurons ameliorate seizures and abnormal behavior in epileptic mice. Cell Stem Cell *15*, 559–573.

Cuntz, H., Forstner, F., Borst, A., and Häusser, M. (2010). One rule to grow them all: a general theory of neuronal branching and its practical application. PLoS Comput. Biol. *6*, e1000877.

Defelipe, J. (2011). The evolution of the brain, the human nature of cortical circuits, and intellectual creativity. Front. Neuroanat. *5*, 29.

Di Lullo, E., and Kriegstein, A.R. (2017). The use of brain organoids to investigate neural development and disease. Nat. Rev. Neurosci. *18*, 573–584.

Ebert, D.H., and Greenberg, M.E. (2013). Activity-dependent neuronal signalling and autism spectrum disorder. Nature *493*, 327–337.

Espuny-Camacho, I., Michelsen, K.A., Gall, D., Linaro, D., Hasche, A., Bonnefont, J., Bali, C., Orduz, D., Bilheu, A., Herpoel, A., et al. (2013). Pyramidal neurons derived from human pluripotent stem cells integrate efficiently into mouse brain circuits in vivo. Neuron *77*, 440–456.

Espuny-Camacho, I., Arranz, A.M., Fiers, M., Snellinx, A., Ando, K., Munck, S., Bonnefont, J., Lambot, L., Corthout, N., Omodho, L., et al. (2017). Hallmarks of Alzheimer's Disease in Stem-Cell-Derived Human Neurons Transplanted into Mouse Brain. Neuron *93*, 1066–1081.e8.

Espuny-Camacho, I., Michelsen, K.A., Linaro, D., Bilheu, A., Acosta-Verdugo, S., Herpoel, A., Giugliano, M., Gaillard, A., and Vanderhaeghen, P. (2018). Human Pluripotent Stem-Cell-Derived Cortical Neurons Integrate Functionally into the Lesioned Adult Murine Visual Cortex in an Area-Specific Way. Cell Rep. *23*, 2732–2743.

Eyal, G., Verhoog, M.B., Testa-Silva, G., Deitcher, Y., Lodder, J.C., Benavides-Piccione, R., Morales, J., DeFelipe, J., de Kock, C.P., Mansvelder, H.D., and Segev, I. (2016). Unique membrane properties and enhanced signal processing in human neocortical neurons. eLife *5*, e16553.

Falkner, S., Grade, S., Dimou, L., Conzelmann, K.K., Bonhoeffer, T., Götz, M., and Hübener, M. (2016). Transplanted embryonic neurons integrate into adult neocortical circuits. Nature *539*, 248–253.

Fandel, T.M., Trivedi, A., Nicholas, C.R., Zhang, H., Chen, J., Martinez, A.F., Noble-Haeusslein, L.J., and Kriegstein, A.R. (2016). Transplanted Human Stem Cell-Derived Interneuron Precursors Mitigate Mouse Bladder Dysfunction and Central Neuropathic Pain after Spinal Cord Injury. Cell Stem Cell *19*, 544–557.

Gaspard, N., and Vanderhaeghen, P. (2010). Mechanisms of neural specification from embryonic stem cells. Curr. Opin. Neurobiol. *20*, 37–43.

Gaspard, N., Bouschet, T., Hourez, R., Dimidschstein, J., Naeije, G., van den Ameele, J., Espuny-Camacho, I., Herpoel, A., Passante, L., Schiffmann, S.N., et al. (2008). An intrinsic mechanism of corticogenesis from embryonic stem cells. Nature *455*, 351–357.

Geschwind, D.H., and Rakic, P. (2013). Cortical evolution: judge the brain by its cover. Neuron *80*, 633–647.

Goldey, G.J., Roumis, D.K., Glickfeld, L.L., Kerlin, A.M., Reid, R.C., Bonin, V., Schafer, D.P., and Andermann, M.L. (2014). Removable cranial windows for long-term imaging in awake mice. Nat. Protoc. *9*, 2515–2538.

Gould, S.J. (1992). Ontogeny and phylogeny–revisited and reunited. BioEssays *14*, 275–279.

Grutzendler, J., Kasthuri, N., and Gan, W.B. (2002). Long-term dendritic spine stability in the adult cortex. Nature *420*, 812–816.

Hofer, S.B., Mrsic-Flogel, T.D., Bonhoeffer, T., and Hübener, M. (2009). Experience leaves a lasting structural trace in cortical circuits. Nature *457*, 313–317.

Holtmaat, A., and Svoboda, K. (2009). Experience-dependent structural synaptic plasticity in the mammalian brain. Nat. Rev. Neurosci. *10*, 647–658.

Holtmaat, A.J., Trachtenberg, J.T., Wilbrecht, L., Shepherd, G.M., Zhang, X., Knott, G.W., and Svoboda, K. (2005). Transient and persistent dendritic spines in the neocortex in vivo. Neuron *45*, 279–291.

Holtmaat, A., Wilbrecht, L., Knott, G.W., Welker, E., and Svoboda, K. (2006). Experience-dependent and cell-type-specific spine growth in the neocortex. Nature *441*, 979–983.

Huo, H.Q., Qu, Z.Y., Yuan, F., Ma, L., Yao, L., Xu, M., Hu, Y., Ji, J., Bhattacharyya, A., Zhang, S.C., and Liu, Y. (2018). Modeling Down Syndrome with Patient iPSCs Reveals Cellular and Migration Deficits of GABAergic Neurons. Stem Cell Reports *10*, 1251–1266.

Hutsler, J.J., and Zhang, H. (2010). Increased dendritic spine densities on cortical projection neurons in autism spectrum disorders. Brain Res. *1309*, 83–94.

Huttenlocher, P.R. (1979). Synaptic density in human frontal cortex - developmental changes and effects of aging. Brain Res. *163*, 195–205.

Huttenlocher, P.R., de Courten, C., Garey, L.J., and Van der Loos, H. (1982). Synaptogenesis in human visual cortex–evidence for synapse elimination during normal development. Neurosci. Lett. *33*, 247–252.

Huttenlocher, P.R., De Courten, C., Garey, L.J., and Van der Loos, H. (1982–1983). Synaptic development in human cerebral cortex. Int. J. Neurol. *16-17*, 144–154.

Jacobs, B., Driscoll, L., and Schall, M. (1997). Life-span dendritic and spine changes in areas 10 and 18 of human cortex: a quantitative Golgi study. J. Comp. Neurol. *386*, 661–680.

Jacobs, B., Schall, M., Prather, M., Kapler, E., Driscoll, L., Baca, S., Jacobs, J., Ford, K., Wainwright, M., and Treml, M. (2001). Regional dendritic and spine variation in human cerebral cortex: a quantitative golgi study. Cereb. Cortex *11*, 558–571.

Jiang, X., Shen, S., Cadwell, C.R., Berens, P., Sinz, F., Ecker, A.S., Patel, S., and Tolias, A.S. (2015). Principles of connectivity among morphologically defined cell types in adult neocortex. Science *350*, aac9462.

Jin, D.Z., Zhao, T., Hunt, D.L., Pearcy, R., Hsu, C.-L., and Spruston, N. (2019). ShuTu: Open-Source Software for Efficient and Accurate Reconstruction of Dendritic Morphology. bioRxiv. https://doi.org/10.1101/226548.

Lancaster, M.A., and Knoblich, J.A. (2014). Organogenesis in a dish: modeling development and disease using organoid technologies. Science *345*, 1247125.

Liu, X., Somel, M., Tang, L., Yan, Z., Jiang, X., Guo, S., Yuan, Y., He, L., Oleksiak, A., Zhang, Y., et al. (2012). Extension of cortical synaptic

development distinguishes humans from chimpanzees and macaques. Genome Res. *22*, 611–622.

Liu, X., Han, D., Somel, M., Jiang, X., Hu, H., Guijarro, P., Zhang, N., Mitchell, A., Halene, T., Ely, J.J., et al. (2016). Disruption of an Evolutionarily Novel Synaptic Expression Pattern in Autism. PLoS Biol. *14*, e1002558.

Lui, J.H., Hansen, D.V., and Kriegstein, A.R. (2011). Development and evolution of the human neocortex. Cell *146*, 18–36.

Mansour, A.A., Gonçalves, J.T., Bloyd, C.W., Li, H., Fernandes, S., Quang, D., Johnston, S., Parylak, S.L., Jin, X., and Gage, F.H. (2018). An in vivo model of functional and vascularized human brain organoids. Nat. Biotechnol. *36*, 432–441.

Marchetto, M.C., Hrvoj-Mihic, B., Kerman, B.E., Yu, D.X., Vadodaria, K.C., Linker, S.B., Narvaiza, I., Santos, R., Denli, A.M., Mendes, A.P., et al. (2019). Species-specific maturation profiles of human, chimpanzee and bonobo neural cells. eLife *8*, e37527.

Maroof, A.M., Keros, S., Tyson, J.A., Ying, S.-W., Ganat, Y.M., Merkle, F.T., Liu, B., Goulburn, A., Stanley, E.G., Elefanty, A.G., et al. (2013). Directed differentiation and functional maturation of cortical interneurons from human embryonic stem cells. Cell Stem Cell *12*, 559–572.

Mazurek, M., Kager, M., and Van Hooser, S.D. (2014). Robust quantification of orientation selectivity and direction selectivity. Front. Neural Circuits *8*, 92.

Michelsen, K.A., Acosta-Verdugo, S., Benoit-Marand, M., Espuny-Camacho, I., Gaspard, N., Saha, B., Gaillard, A., and Vanderhaeghen, P. (2015). Area-specific reestablishment of damaged circuits in the adult cerebral cortex by cortical neurons derived from mouse embryonic stem cells. Neuron *85*, 982–997.

Mizuno, H., Ikezoe, K., Nakazawa, S., Sato, T., Kitamura, K., and Iwasato, T. (2018). Patchwork-Type Spontaneous Activity in Neonatal Barrel Cortex Layer 4 Transmitted via Thalamocortical Projections. Cell Rep. *22*, 123–135.

Mrzljak, L., Uylings, H.B., Van Eden, C.G., and Judás, M. (1990). Neuronal development in human prefrontal cortex in prenatal and postnatal stages. Prog. Brain Res. *85*, 185–222.

Murmu, R.P., Li, W., Holtmaat, A., and Li, J.Y. (2013). Dendritic spine instability leads to progressive neocortical spine loss in a mouse model of Huntington's disease. J. Neurosci. *33*, 12997–13009.

Nagashima, F., Suzuki, I.K., Shitamukai, A., Sakaguchi, H., Iwashita, M., Kobayashi, T., Tone, S., Toida, K., Vanderhaeghen, P., and Kosodo, Y. (2014). Novel and robust transplantation reveals the acquisition of polarized processes by cortical cells derived from mouse and human pluripotent stem cells. Stem Cells Dev. *23*, 2129–2142.

Nevian, T., and Sakmann, B. (2006). Spine Ca2+ signaling in spike-timing-dependent plasticity. J. Neurosci. *26*, 11001–11013.

Nicholas, C.R., Chen, J., Tang, Y., Southwell, D.G., Chalmers, N., Vogt, D., Arnold, C.M., Chen, Y.J.J., Stanley, E.G., Elefanty, A.G., et al. (2013). Functional maturation of hPSC-derived forebrain interneurons requires an extended timeline and mimics human neural development. Cell Stem Cell *12*, 573–586.

Niell, C.M., and Stryker, M.P. (2008). Highly selective receptive fields in mouse visual cortex. J. Neurosci. *28*, 7520–7536.

Noakes, Z., Keefe, F., Tamburini, C., Kelly, C.M., Cruz Santos, M., Dunnett, S.B., Errington, A.C., and Li, M. (2019). Human Pluripotent Stem Cell-Derived Striatal Interneurons: Differentiation and Maturation In Vitro and in the Rat Brain. Stem Cell Reports *12*, 191–200.

Petanjek, Z., Judaš, M., Šimic, G., Rasin, M.R., Uylings, H.B., Rakic, P., and Kostovic, I. (2011). Extraordinary neoteny of synaptic spines in the human prefrontal cortex. Proc. Natl. Acad. Sci. USA *108*, 13281–13286.

Pfeiffer, B.E., Zang, T., Wilkerson, J.R., Taniguchi, M., Maksimova, M.A., Smith, L.N., Cowan, C.W., and Huber, K.M. (2010). Fragile X mental retardation protein is required for synapse elimination by the activity-dependent transcription factor MEF2. Neuron *66*, 191–197.

Qi, Y., Zhang, X.J., Renier, N., Wu, Z., Atkin, T., Sun, Z., Ozair, M.Z., Tchieu, J., Zimmer, B., Fattahi, F., et al. (2017). Combined small-molecule inhibition accelerates the derivation of functional cortical neurons from human pluripotent stem cells. Nat. Biotechnol. *35*, 154–163.

Rakic, P., Bourgeois, J.P., Eckenhoff, M.F., Zecevic, N., and Goldman-Rakic, P.S. (1986). Concurrent overproduction of synapses in diverse regions of the primate cerebral cortex. Science *232*, 232–235.

Real, R., Peter, M., Trabalza, A., Khan, S., Smith, M.A., Dopp, J., Barnes, S.J., Momoh, A., Strano, A., Volpi, E., et al. (2018). In vivo modeling of human neuron dynamics and Down syndrome. Science *362*, eaau1810.

Reardon, T.R., Murray, A.J., Turi, G.F., Wirblich, C., Croce, K.R., Schnell, M.J., Jessell, T.M., and Losonczy, A. (2016). Rabies Virus CVS-N2c(ΔG) Strain Enhances Retrograde Synaptic Transfer and Neuronal Viability. Neuron *89*, 711–724.

Rochefort, N.L., Narushima, M., Grienberger, C., Marandi, N., Hill, D.N., and Konnerth, A. (2011). Development of direction selectivity in mouse cortical neurons. Neuron *71*, 425–432.

Schindelin, J., Arganda-Carreras, I., Frise, E., Kaynig, V., Longair, M., Pietzsch, T., Preibisch, S., Rueden, C., Saalfeld, S., Schmid, B., et al. (2012). Fiji: an open-source platform for biological-image analysis. Nat. Methods *9*, 676–682.

Shi, Y., Kirwan, P., Smith, J., Robinson, H.P.C., and Livesey, F.J. (2012). Human cerebral cortex development from pluripotent stem cells to functional excitatory synapses. Nat. Neurosci. *15*, 477–486, S1.

Sousa, A.M.M., Meyer, K.A., Santpere, G., Gulden, F.O., and Sestan, N. (2017). Evolution of the Human Nervous System Function, Structure, and Development. Cell *170*, 226–247.

Southwell, D.G., Nicholas, C.R., Basbaum, A.I., Stryker, M.P., Kriegstein, A.R., Rubenstein, J.L., and Alvarez-Buylla, A. (2014). Interneurons from embryonic development to cell-based therapy. Science *344*, 1240622.

Spires-Jones, T.L., and Hyman, B.T. (2014). The intersection of amyloid beta and tau at synapses in Alzheimer's disease. Neuron *82*, 756–771.

Suzuki, I.K., and Vanderhaeghen, P. (2015). Is this a brain which I see before me? Modeling human neural development with pluripotent stem cells. Development *142*, 3138–3150.

Suzuki, I.K., Gacquer, D., Van Heurck, R., Kumar, D., Wojno, M., Bilheu, A., Herpoel, A., Lambert, N., Cheron, J., Polleux, F., et al. (2018). Human-Specific NOTCH2NL Genes Expand Cortical Neurogenesis through Delta/Notch Regulation. Cell *173*, 1370–1384.e16.

Tabar, V., and Studer, L. (2014). Pluripotent stem cells in regenerative medicine: challenges and recent progress. Nat. Rev. Genet. *15*, 82–92.

Takashima, S., Becker, L.E., Armstrong, D.L., and Chan, F. (1981). Abnormal neuronal development in the visual cortex of the human fetus and infant with down's syndrome. A quantitative and qualitative Golgi study. Brain Res. *225*, 1–21.

Testa-Silva, G., Verhoog, M.B., Linaro, D., de Kock, C.P.J., Baayen, J.C., Meredith, R.M., De Zeeuw, C.I., Giugliano, M., and Mansvelder, H.D. (2014). High bandwidth synaptic communication and frequency tracking in human neocortex. PLoS Biol. *12*, e1002007.

Thomson, J.A., Itskovitz-Eldor, J., Shapiro, S.S., Waknitz, M.A., Swiergiel, J.J., Marshall, V.S., and Jones, J.M. (1998). Embryonic stem cell lines derived from human blastocysts. Science *282*, 1145–1147.

Ting, J.T., Daigle, T.L., Chen, Q., and Feng, G. (2014). Acute Brain Slice Methods for Adult and Aging Animals: Application of Targeted Patch Clamp Analysis and Optogenetics. In Patch-Clamp Methods and Protocols, M. Martina and S. Taverna, eds. (Springer), pp. 221–242.

Tjia, M., Yu, X., Jammu, L.S., Lu, J., and Zuo, Y. (2017). Pyramidal Neurons in Different Cortical Layers Exhibit Distinct Dynamics and Plasticity of Apical Dendritic Spines. Front. Neural Circuits *11*, 43.

Tornero, D., Wattananit, S., Grønning Madsen, M., Koch, P., Wood, J., Tatarishvili, J., Mine, Y., Ge, R., Monni, E., Devaraju, K., et al. (2013). Human induced pluripotent stem cell-derived cortical neurons integrate in stroke-injured cortex and improve functional recovery. Brain *136*, 3561–3577.

Tornero, D., Tsupykov, O., Granmo, M., Rodriguez, C., Grønning-Hansen, M., Thelin, J., Smozhanik, E., Laterza, C., Wattananit, S., Ge, R., et al. (2017).

Synaptic inputs from stroke-injured brain to grafted human stem cell-derived neurons activated by sensory stimuli. Brain *140*, 692–706.

Trachtenberg, J.T., Chen, B.E., Knott, G.W., Feng, G., Sanes, J.R., Welker, E., and Svoboda, K. (2002). Long-term in vivo imaging of experience-dependent synaptic plasticity in adult cortex. Nature *420*, 788–794.

Trujillo, C.A., Gao, R., Negraes, P.D., Gu, J., Buchanan, J., Preissl, S., Wang, A., Wu, W., Haddad, G.G., Chaim, I.A., et al. (2019). Complex Oscillatory Waves Emerging from Cortical Organoids Model Early Human Brain Network Development. Cell Stem Cell *25*, 558–569 e557.

van den Ameele, J., Tiberi, L., Vanderhaeghen, P., and Espuny-Camacho, I. (2014). Thinking out of the dish: what to learn about cortical development using pluripotent stem cells. Trends Neurosci. *37*, 334–342.

Wekselblatt, J.B., Flister, E.D., Piscopo, D.M., and Niell, C.M. (2016). Large-scale imaging of cortical dynamics during sensory perception and behavior. J. Neurophysiol. *115*, 2852–2866.

Willsey, A.J., Sanders, S.J., Li, M., Dong, S., Tebbenkamp, A.T., Muhle, R.A., Reilly, S.K., Lin, L., Fertuzinhos, S., Miller, J.A., et al. (2013). Coexpression networks implicate human midfetal deep cortical projection neurons in the pathogenesis of autism. Cell *155*, 997–1007.

Wolf, F.A., Angerer, P., and Theis, F.J. (2018). SCANPY: large-scale single-cell gene expression data analysis. Genome Biol. *19*, 15.

Ying, Q.L., Nichols, J., Evans, E.P., and Smith, A.G. (2002). Changing potency by spontaneous fusion. Nature *416*, 545–548.

Zeltner, N., and Studer, L. (2015). Pluripotent stem cell-based disease modeling: current hurdles and future promise. Curr. Opin. Cell Biol. *37*, 102–110.

Zoghbi, H.Y., and Bear, M.F. (2012). Synaptic dysfunction in neurodevelopmental disorders associated with autism and intellectual disabilities. Cold Spring Harb. Perspect. Biol. *4*, a009886.

Zuo, Y., Lin, A., Chang, P., and Gan, W.B. (2005). Development of long-term dendritic spine stability in diverse regions of cerebral cortex. Neuron *46*, 181–189.

STAR★METHODS

KEY RESOURCES TABLE

REAGENT or RESOURCE	SOURCE	IDENTIFIER
Antibodies		
Chicken polyclonal anti-GFP	abcam	Cat# ab13970
Rabbit polyclonal anti-RFP	Rockland	Cat# 600-401-379
Mouse monoclonal anti-Tubulin β3 (Tuj1)	Covance	Cat# MMS-435P
Goat polyclonal anti-Sox2	Santa Cruz	Cat# sc-17320
Rabbit monoclonal anti-TBR1 [EPR8138(2)]	abcam	Cat# ab183032
Rat monoclonal anti-Ctip2 [25B6]	abcam	Cat# ab18465
Mouse monoclonal anti-Human Nuclei [235-1]	MERCK	Cat# MAB1281
Rabbit polyclonal anti-BF1 (FOXG1)	Takara bio	Cat# M227
Rabbit polyclonal anti-FOXP2	abcam	Cat# ab16046
Rabbit polyclonal anti-SATB2	abcam	Cat# ab34735
Rabbit polyclonal anti-CDP (CUX1)	Santa Cruz	Cat# sc-13024
Mouse monoclonal anti-NeuN	Sigma-Aldrich	MAB377
Mouse monoclonal anti-APC	Sigma-Aldrich	OP80
Mouse monoclonal anti-GAD67	Sigma-Aldrich	MAB5406
Rabbit polyclonal anti-Nestin	BioLegend	839801
Alexa Fluor® 488 AffiniPure Donkey Anti-Chicken IgY (IgG) (H+L)	Jackson ImmunoResearch	Cat# 703-545-155
Alexa Fluor® 488 AffiniPure Donkey Anti-Mouse IgG (H+L)	Jackson ImmunoResearch	Cat#: 715-545-150
Cy3 AffiniPure Donkey Anti-Rabbit IgG (H+L)	Jackson ImmunoResearch	Cat# 711-165-152
Cy3 AffiniPure Donkey Anti-Rat IgG (H+L)	Jackson ImmunoResearch	Cat# 712-165-153
Cy3 AffiniPure Donkey Anti-Mouse IgG (H+L)	Jackson ImmunoResearch	Cat# 715-165-150
Alexa Fluor® 647 AffiniPure Donkey Anti-Rabbit IgG (H+L)	Jackson ImmunoResearch	Cat# 711-605-152
Alexa Fluor® 647 AffiniPure Donkey Anti-Mouse IgG (H+L)	Jackson ImmunoResearch	Cat# 715-605-151
Alexa Fluor® 647 AffiniPure Donkey Anti-Goat IgG (H+L)	Jackson ImmunoResearch	Cat# 705-605-147
Bacterial and Virus Strains		
Lenti-hSynI-EmGFP-WPRE	This study	N/A
Lenti-CAG-Venus-WPRE	This study	N/A
Lenti-hSynI-Venus-WPRE	This study	N/A
Lenti-hSynI-TVA-mCherry-P2A-N2c(G)-WPRE	This study	N/A
Lenti-TRE-GCaMP6s-P2A-nls-dTomato-WPRE	This study	N/A
Lenti-UbC-M2rtTA-WPRE	This study	N/A
CVS-N2CdG-eGFP	This study	N/A
Chemicals, Peptides, and Recombinant Proteins		
ROCK inhibitor (Y-27632)	MERCK	Cat# 688000
Recombinant human Noggin	R&D systems	Cat# 1967-NG
Doxycycline hydrochloride	MERCK	Cat# D3447
Knockout DMEM	Thermo Fisher Scientific	Cat# 10829018
Knockout Serum Replacer	Thermo Fisher Scientific	Cat# 10828028
Non-essential Amino Acids	Thermo Fisher Scientific	Cat# 11140050
Penicillin/Streptomycin	Thermo Fisher Scientific	Cat# 15070063
2-Mercaptoenthanol	MERCK	Cat# M6250
L-glutamine	Thermo Fisher Scientific	Cat# 25030081
Dispase II, powder	Thermo Fisher Scientific	Cat# 17105041

(*Continued on next page*)

Continued

REAGENT or RESOURCE	SOURCE	IDENTIFIER
Collagenase, Type IV, powder	Thermo Fisher Scientific	Cat# 17104019
Stem-Pro Accutase	Thermo Fisher Scientific	Cat# A1110501
Matrigel hES qualified	BD	Cat# 354277
B-27 Supplement (50X), minus vitamin A	Thermo Fisher Scientific	Cat# 12587010
X-tremeGENE HP DNA Transfection Reagent	MERCK	Cat# 6366244001
mFreSR	STEMCELL Tech	Cat# 05855
DAPT, gamma-Secretase inhibitor	abcam	Cat# ab120633
Cytarabine	MERCK	Cat# C3350000
Ethylene glycol-bis(2-aminoethylether)-N,N,N′, N′-tetraacetic acid	MERCK	Cat# 03777
Fast Green	MERCK	Cat# 210-M
$CaCl_2$	Sigma-Aldrich	C5670
Na-ascorbate	Sigma-Aldrich	A4034
Na-pyruvate	Sigma-Aldrich	P8574
NaCl	Sigma-Aldrich	71376
KCl	Sigma-Aldrich	P9541
NaH_2PO_4	Sigma-Aldrich	S7907
$MgCl_2$	Sigma-Aldrich	M8266
$MgSO_4$	Sigma-Aldrich	M7506
N-Methyl-D-glucamine	Sigma-Aldrich	M2004
Thiourea	Sigma-Aldrich	T8656
D-glucose	Sigma-Aldrich	D9434
$NaHCO_3$	Sigma-Aldrich	S6297
HEPES	Sigma-Aldrich	54457
SR95531 (Gabazine)	Sigma-Aldrich	S106
Potassium D-gluconate	Sigma-Aldrich	G4500
ATP-Mg	Sigma-Aldrich	A9187
GTP-Na_2	Sigma-Aldrich	G8877
Na_2-phosphocreatine	Sigma-Aldrich	P7936
Biocytin	Sigma-Aldrich	B4261
Experimental Models: Cell Lines		
Human embryonic stem cell H9	WiCell	Cat# NIHhESC-10-0062
Experimental Models: Organisms/Strains		
Mouse: NOD-Scid	JANVIER LABS	NOD.CB-17-Prkdc scid
Mouse: RAG2 KO	Jackson Laboratories	B6(Cg)-*Rag2*$^{tm1.1Cgn}$/J
Mouse: GCaMP6s line	Jackson Laboratories	CaMKII-tTA x TRE-GCaMP6 line G6s2
Mouse: tdTomato reporter	Jackson Laboratories	Emx1-Cre x Rosa-CAG-LSL-tdTomato-WPRE
Recombinant DNA		
pMD2.G	Didier Trono	Addgene:12259
psPAX2	Didier Trono	Addgene:12260
FUW-M2rtTA	Rudolf Jaenisch	Addgene:20342
AAV-hSyn1-GCaMP6s-P2A-nls-dTomato	Jonathan Ting	Addgene: 51084
AAV-CaMKII-GCaMP6f-WPRE-SV40	UPenn	AV-5-PV3435
CAG-FLEx(FRT)-TC	Liqun Luo	Addgene: 67827
pCAGGS-N2c(G)	Thomas Jessell	Addgene: 73481
mEmerald-Mito-7	Michael Davidson	Addgene: 54160
pLenti-hSynI-EmGFP-WPRE	This study	N/A
pLenti-CAG-Venus-WPRE	This study	N/A

(*Continued on next page*)

Continued

REAGENT or RESOURCE	SOURCE	IDENTIFIER
pLenti-hSynI-Venus-WPRE	This study	N/A
pLenti-hSynI-TVA-mCherry-P2A-N2c(G)-WPRE	This study	N/A
pLenti-TRE-GCaMP6s-P2A-nls-dTomato-WPRE	This study	N/A
Software and Algorithms		
Imaris	Bitplane	RRID:SCR_007370
ImageJ	N/A	RRID:SCR_002285
ShuTu	N/A	DOI:10.1101/226548
Custom-written MATLAB routines	This study	N/A
SCANPY	Wolf et al., 2018	https://doi.org/10.1186/s13059-017-1382-0

LEAD CONTACT AND MATERIALS AVAILABILITY

Further information and requests for resources and reagents should be directed to and will be fulfilled by the Lead Contact at pierre.vanderhaeghen@kuleuven.vib.be.

EXPERIMENTAL MODEL AND SUBJECT DETAILS

Animals

All mouse experiments were performed with the approval of the KULeuven and ULB Committees for animal welfare. Animals were housed under standard conditions (12 h light:12 h dark cycles) with food and water *ad libitum*. Data for this study are derived from a total of 65 mice of both sexes.

METHOD DETAILS

Human ESC differentiation into cortical cells

Human ESC H9 (Thomson et al., 1998) and H9-GFP (Espuny-Camacho et al., 2013) cells were maintained on irradiated mouse embryonic fibroblasts (MEF) in the ES medium until the start of cortical differentiation. Cortical differentiation from human ESC was performed as described previously (Espuny-Camacho et al., 2013) with some modifications (Suzuki et al., 2018). On day −2, ESCs were dissociated using Stem-Pro Accutase (Thermo Fisher Scientific, Cat#A1110501) and plated on matrigel- (hES qualified matrigel BD, Cat#354277) coated dishes at low confluency (5,000–10,000 cells/cm2) in MEF-conditioned hES medium supplemented with 10 μM ROCK inhibitor (Y-27632; Merck, Cat#688000). On day 0 of the differentiation, the medium was changed to DDM (Gaspard et al., 2008), supplemented with B27 devoid of Vitamin A (Thermo Fisher Scientific, Cat#12587010) and 100 ng/ml Noggin (R&D systems, Cat#1967-NG), and the medium was changed every 2 days until day 6. From day 6, the medium was changed every day until day 16. After day 16 of differentiation, the medium was changed to DDM, supplemented with B27 (DDM/B27), and changed every day. At day 25, the progenitors were dissociated using Accutase and cryopreserved in mFreSR (StemCell Technologies, Cat#05855).

For comparison cortical neurons derived with another protocol, cortical differentiation was performed as in Shi et al. (2012).

Differentiated cortical cells were validated for neuronal and cortical markers by immunostaining using antibodies for TUBB3 (BioLegend, Cat#MMS-435P), TBR1 (Abcam, Cat#ab183032), CTIP2 (Abcam, Cat#ab18465), FOXG1 (Takara, Cat#M227), Sox2 (Santa Cruz, Cat#sc-17320), FOXP2 (Abcam, Cat#ab16046), SATB2 (Abcam, Cat#ab34735), CUX1 (Santa Cruz, Cat#sc-13024), NeuN (Sigma-Aldrich, Cat#MAB377), APC (Sigma-Aldrich, Cat#OP80), GAD67 (Sigma-Aldrich, Cat#MAB5406), and Nestin (BioLegend, Cat#839801).

Viral constructs

HEK293T cells were transfected by packaging plasmids, psPAX2 (Addgene Cat#12260) and pMD2.G (Addgene Cat#12259), and a plasmid of gene of interest in lentiviral backbone (pLenti-hSynapsin I promoter-EmGFP-WPRE, pLenti-CAG-Venus-WPRE, pLenti-hSynapsin I promoter-Venus-WPRE, pLenti-hSynapsin I promoter-TVA-mCherry–P2A–N2c(G) -WPRE, pLenti-TRE-GCaMP6s-P2A-nls-dTomato-WPRE and FUW-M2rtTA (Addgene Cat#20342)). 3 days after transfection, culture medium was collected and viral particles were enriched by filter device (Amicon Ultra-15 Centrifuge Filters, Merck, Cat#UFC910008). Titer check was performed on HEK293T cell culture for every batch of lentiviral preparation.

Neonatal transplantation

Human cortical cells that were frozen at day 25, were thawed and plated on matrigel-coated plates using DDM/B27 and Neurobasal supplemented with B27 (DDM/B27+Nb/B27) medium. Seven days after plating, cells were dissociated using Accutase and plated on

new matrigel-coated plates at high confluency (100,000–600,000 cells/cm^2) with or without lentiviral vector. The following day, medium was changed to DDM/B27+Nb/B27 medium. At 14-16 days after thawing, cells were treated with 10 μM DAPT (Abcam, Cat#ab120633) for 24 hours. The following day, cells were treated with 5 μM Cytarabine (Merck, Cat#C3350000) for 24 hours. At day 17-19 days after thawing, cells were dissociated using Accutase and suspended in the injection solution containing 20 mM EGTA (Merck, Cat#03777) and 0.1% Fast Green (Merck, Cat#210-M) in PBS at 40,000–200,000 cells/μl. Approximately 1-2 μl of cell suspension was injected into the lateral ventricles of each hemisphere of neonatal (postnatal day 0 or 1) immunodeficient mice (NOD/SCID or $Rag2^{-/-}$) using glass capillaries pulled on a horizontal puller (Sutter P-97).

For lentiviral infection experiments, the absence of infection of the host cells was confirmed by co-staining for lentiviral marker (GFP or tdTomato) and human nuclear antigen (MERCK Cat#MAB1281), which revealed 100% co-labeling at 2 MPT (Figure S1).

FACS and scRNA-seq of transplanted cells

Transplanted cells were enriched via FACS for eGFP from the cerebral cortex of transplanted animals at 2 MPT. Cells were sorted using a BD Influx with a 100 μm nozzle at 18psi and eGFP was detected using a 200 mW 488 nm laser with a 530/40 BP filter.

Single cells were processed using the 10X Chromium Single Cell 3′ V3 kit across 2 lanes following manufacturers guidelines and were sequenced using an Illumina HiSeq4000. Data was first processed using CellRanger 3.0.2 with a combined human/mouse index generated using Illumina iGenomes databases, the resulting cells were then further filtered using the Scanpy (Wolf et al., 2018) package, removing cells with less than 1000 genes detected and finally removing genes detected in less than 3 cells. The sum of all remaining genes for each species was then determined per cell.

Electrophysiology

Whole-cell patch-clamp recordings were performed intracellularly on grafted neurons in acute brain slices from mice starting at 1 and up to 11 MPT, as previously described (Espuny-Camacho et al., 2013). Briefly, transplanted mice were lightly anaesthetized with isofluorane and decapitated. Alternatively, animals older than 3 months were anaesthetized intraperitoneally with Nembutal and transcardially perfused with ~20 mL of ice-cold NMDG-based slicing solution (Jiang et al., 2015; Ting et al., 2014). Brains were rapidly extracted and placed in ice-cold NMDG-based slicing solution containing (in mM): 93 *N*-Methyl-D-glucamine, 2.5 KCl, 1.2 NaH_2PO_4, 0.5 $CaCl_2$, 10 $MgSO_4$, 30 $NaHCO_3$, 5 Na-ascorbate, 3 Na-pyruvate, 2 Thiourea, 20 HEPES and 25 D-glucose (pH adjusted to 7.35 with 10 N HCl, gassed with 95% O_2/5% CO_2). The cerebellum and hindbrain were trimmed and the remaining block of tissue was glued onto the slicing platform of a Leica VT1200. 250-300 μm thick coronal slices were cut in ice-cold NMDG-based slicing solution and subsequently incubated for ~10 minutes in the same solution at 34°C. Slices were then stored for at least 45 minutes at room temperature in standard aCSF, containing (in mM): 125 NaCl, 2.5 KCl, 1.25 NaH_2PO_4, 2 $CaCl_2$, 1 $MgCl_2$, 30 $NaHCO_3$ and 25 D-glucose (gassed with 95% O_2/5% CO_2). For the experiments shown in Figures S2F–S2K, brains from adult animals (P40-42) were dissected in NMDG as described, whereas brains from juvenile animals (P14-15) were dissected and slices were cut in standard ice-cold aCSF. Slices were then incubated for 45 minutes in aCSF at 34°C before being stored at room temperature for up to 8 hours. For recording one slice at a time was transferred to a chamber and continuously perfused with aCSF at ~1 ml/min. Transplanted cells were identified by their EGFP fluorescence and visualized using an upright microscope equipped with infrared differential interference contrast (Carl Zeiss NV, Belgium).

Rabies virus-based monosynaptic tracing

For rabies-based monosynaptic tracing, human cortical cells frozen at day 25 were thawed and infected *in vitro* with lenti-hSynI-TVA-mCherry-P2A-N2c(G) at day 32 (transfection efficiency ~50%). Cells were subsequently transplanted at day 41 as described above. At approximately 3 MPT, n = 2 NOD/SCID mice were anaesthetized with isoflurane (2.5%–3% induction, 1%–1.25% maintenance) and a small craniotomy approximately 2 mm in diameter targeting barrel cortex was performed 0.7 mm posterior and 3.5 mm lateral from Bregma. Approximately 200 nL of rabies virus (N2c ΔG-eGFP(EnvA)) (Reardon et al., 2016) were injected using a bevelled glass capillary mounted on a Nanoject II injector (Drummond Scientific) at a depth of 0.45 mm from the brain surface at a rate of 18.4 nL per injection with ~30 s between injections. After 2 weeks, animals were perfused with freshly prepared 4% paraformaldehyde (Invitrogen) and subsequent histology was performed as described in the Immunofluorescence section.

Surgical procedures

Standard craniotomy surgeries were performed to gain optical access to the visual cortex through a set of cover glasses (Goldey et al., 2014). Rag2KO mice aging between 2 and 6 months were anaesthetized (isoflurane 2.5%–3% induction, 1%–1.25% or a mix of ketamine and xylazine 100 mg/kg and 10 mg/kg respectively). A custom-made titanium head plate was mounted to the skull, and a craniotomy over the visual cortex was made for calcium imaging. The craniotomy was covered with a cranial window, which was constructed by bonding two 4 or 5 mm cover glass to a larger (7 mm) top cover glass using optical adhesive (NOA 71, Norland). Buprenex and Cefazolin were administered postoperatively (2 mg/kg and 5 mg/kg respectively) when the animal recovered from anaesthesia and these injections were repeated every 12 hours for 3 days after surgery.

Widefield calcium imaging

Widefield fluorescent images were acquired through a 2x objective (NA = 0.055, Edmund Optics). Illumination was from a blue LED (479 nm, ThorLabs), the green fluorescence was collected with an EMCCD camera (EM-C2, QImaging) via a bandpass filter (510/84 nm filter, Semrock). The image acquisition was controlled with customized software written in Python.

Two-photon calcium imaging

A customized two-photon microscopy (Neurolabware) was used. GCaMP6s were excited at 920 nm wavelength with a Ti:Sapphire excitation laser (MaiTai eHP DeepSee, Spectra-Physics). The emitted photons were split by a dichroic beamsplitter (centered at 562 nm) and collected with a photomultiplier tube (PMT, Hamamatsu) through a bandpass filter (510 ± 42 nm, Semrock) for the green fluorescence of GFP or GCaMP6s and a bandpass filter (607 ± 35 nm, Semrock) for the red fluorescence of nls-dTomato.

In vivo structural imaging

Animals were anaesthetized using a mix of ketamine (100 mg/kg) and xylazine (10 mg/kg) at 1% ml/g of their body weight. They were placed on a sterilized plexiglass platform and protective eye ointment was applied to both eyes.

The high NA objective (25x Olympus, 1.05 NA) was aligned to be orthogonal to the surface of the top coverslip. All imaging was performed by moving the motorized stages of the microscope along a virtual axis parallel to the optical axis of the objective. We acquired high resolution anatomical stacks from anaesthetized mice. Typical stacks consisted of 200-300 optical section spaced 1 μm apart. The imaged area spanned 75x120 μm. To reduce effects of shot noise, we averaged over 50 frames collected per section and applied a 3D median filter (Fiji, kernel size = [1.5, 1.5, 4]) over the entire stack. Using these preprocessed stacks, we traced branches of interest using a custom MATLAB GUI. We then extracted 3D sub-volumes (10 × 10 x X μm, where X is the length of the branch, ranging 50-120 μm) that were rotated in all 3 dimensions to closely fit each branch. These sub-volumes were used for subsequent analysis.

In vivo functional imaging

To enable functional imaging of transplanted human cells, these were infected *in vitro* with both LV-TRE-GCaMP6s-P2A-nls-dTomato-WPRE and LV-UbC-M2rtTA-WPRE two weeks ahead of transplantation. In these conditions, 50%–70% cells express both GCaMP6s and nls-dTomato under doxycycline treatment.

Two-photon images (702x796 pixels per frame) were collected at 20 Hz with a 16x objective (Nikon 0.80 NA). Volume imaging was accomplished by using an electro-tunable lens (EL-10-30-TC, Optotune) to move the focal plane using a sawtooth pattern in 4 or 5 steps (50 μm separation). We simultaneously recorded neuronal activities in large volumes (1 × 1.5 × 0.20 mm^3) of layer 2/3 visual cortex. During imaging, mice were head-clamped on a sterile plexiglass platform while consciously viewing the visual stimuli on the display. Eye movements were monitors using a camera and infrared illumination (720–900 nm bandpass filters, Edmund).

Visual stimuli were displayed on a gamma-corrected LCD display (22″″, Samsung 2233RZ). The screen was oriented parallel to the eye and placed 18 cm from the animal (covering 80 degrees in elevation by 105 degrees in azimuth). Spherical correction was applied to the stimuli to define eccentricity in spherical coordinates. Visual stimuli consisted of drifting square wave gratings in 6 combinations of 3 spatial frequencies (SF = 0.04, 0.08, 0.16 cycles per degree) and 2 temporal frequencies (TF = 1, 4 Hz) in 12 directions covering 360 degrees. In an early version of the experiment, gratings (SF = 0.05 cpd and TF = 4 Hz) drifting in 8 directions were presented. We collected a control dataset from the CaMKII-tTA x TRE-GCamp6 line G6s2 transgenic mouse line (Wekselblatt et al., 2016). In two additional transplanted Rag2 KO animals we injected AAV5-CaMKII-GCaMP6f (UPenn) into V1 and imaged responses of host mouse cells.

Immunofluorescence

Mice were fixed by transcardiac perfusion with freshly-prepared 4% paraformaldehyde in PBS (Invitrogen). Brains were dissected, and 100 μm sections were prepared using a Leica VT1000S vibrosector. Slices were transferred into PBS with 0.5 μg/mL sodium azide (Sigma), then blocked with PBS supplemented with 3% horse serum (Invitrogen) and 0.3% Triton X-100 (Sigma) during 1 h, and incubated overnight at 4°C with the primary antibodies. After three washes with PBS/0.1% Triton X-100, slices were incubated in PBS for 1 h at room temperature and incubated 2 h at room temperature with the appropriated secondary antibodies. Sections were again washed three times with PBS/0.1% Triton X-100, stained with Hoechst (bisBenzimide H 33258, Sigma) or DAPI (Sigma) for 60 min and washed twice in PBS. The sections were next mounted on a Superfrost slide (Thermo Scientific) and dried using a brush before adding Glycergel mounting medium (Dako). Imaging was performed using either a Zeiss LSM780 or LSM880 confocal microscope controlled by the Zen Black software (Zeiss).

QUANTIFICATION AND STATISTICAL ANALYSIS

Electrophysiology

All electrophysiological recordings were analyzed using MATLAB (The Mathworks, Natick, MA). Raw voltage traces were filtered at 5 kHz and passive membrane and AP properties were extracted and saved in a database for further analysis and statistics. F-I curves shown in Figure 2E were fitted with a power-law function of the form $f(I) = aI^b + c$.

In vivo spine imaging

Segmented branches for adjacent time points were loaded into a custom GUI and all protrusions where marked as spines. During this process we took the 3D structure of the spine into account by scrolling through the volume. This allowed us to distinguish between actual spines and processes passing above and below the branch of interest. We then correlated spines in both time points using their location relative to branch landmarks. Spines that were present in both time points were marked as *conserved*. Spine present only in the first time point were marked as *lost* and, conversely, spines that were found only in the second time point were marked as *gained*. Spines present on a non-overlapping section of the branch were marked, but only included for the spine density quantification. The spine *density* was calculated by counting the number of actual spines on each segment and dividing this count by the length of the branch. This length was obtained by summing the distances between adjacent markers used to trace the branch. Spine *turn-over* was calculated by dividing the sum of gained and lost spines by the sum of spines present at both time points. The resulting time lapse curves were analyzed using a mixed model ANOVA with age group as between-subject factor and time point as within-subject factor. Spine density for gained and lost spines was calculated by counting gained and lost spines and dividing by branch length. To obtain the survival function, we took all spines present in the first time point (*reference*) and then checked for how many subsequent time points each spine of this set was conserved. Survival fraction for individual time point *t* was then calculated by dividing the total number of surviving spines at time *t* by the total number of spines in the *reference* set.

Calcium imaging

Two-photon movies for all experiments collected during 1 session were motion registered to a common reference image. This image was constructed by registering and then averaging 1200 frames from the center of the session. We manually segmented regions-of-interest (ROIs) using information from both red and green channels. We then extracted cellular time courses for each ROI by averaging all pixels inside each ROI, removing the neuropil signal and correcting for slow baseline drift. We then calculated $\Delta F/F_o$ traces by subtracting the baseline fluorescence (F_o) corrected time course and dividing by F_o.

To quantify activity of neurons, we used an differential algorithm that detected epochs were the calcium trace increased by more than 2x STD/second, where STD is the standard deviation of the distribution constructed by combining the negative part of the trace with its sign-inverted counterpart. Neurons were considered *active* if their calcium trace exhibited more than 0.5 transients per minute. Neurons were deemed *visually responsive* if, for at least one condition, the median response exceeded 3x STD, where STD is the standard deviation of the blank epochs preceding each stimulus epoch for this condition.

For orientation tuning experiment we determined the *orientation selectivity index* (OSI) and *direction selectivity index* (DSI) based on circular variance as proposed by Mazurek 2014 (Mazurek et al., 2014). Neurons with an OSI/DSI > 0.2 were deemed *tuned* for orientation/direction of the drifting grating. For tuned neurons, we calculate the *preferred orientation* as the vector mean of responses to individual directions.

Morphology reconstructions and analysis

At the end of each electrophysiological recording, slices containing a single biocytin-filled cell were placed in freshly-prepared 4% paraformaldehyde and fixed overnight. Slices were stained as described previously, using as primary antibodies chicken anti-GFP (Abcam, 1:2000) and occasionally mouse anti-human nucleus (Merck, 1:500) to confirm the human identity of the recorded cells. Streptavidin conjugate NL557 (R&D Systems, 1:2000) was added to the secondary antibodies, and left to incubate for at least 2 hours at room temperature. Full morphologies were imaged on a Zeiss LSM780 or LSM880 confocal microscope, using 40x (NA 1.3) or 63x (NA 1.4) oil immersion objectives, at a horizontal resolution of 0.088 – 0.138 μm/pixel and a vertical resolution of 0.4 – 0.5 μm/pixel. Zeiss proprietary files were converted to stacks of TIFF files, which were then automatically stitched. The morphologies were reconstructed using the semi-automated procedure provided by ShuTu (Jin et al., 2019), followed by manual curation. Digital representations of cellular morphologies were stored in SWC files and analyzed using the TREES toolbox (Cuntz et al., 2010). The Cell Counter toolbox in FIJI (Schindelin et al., 2012) was used to manually annotate spine positions in 3 dimensions.

Dendritic spines were reconstructed in 3D using Imaris (Bitplane) from distal dendritic branches of L5 pyramidal neurons of a 5-week old mouse and from 10 MPT human neurons.

Statistical analysis

Results are shown as mean ± standard error (SEM) of at least three biologically independent experiments. Electrophysiological properties are shown as median and interquartile range, as indicated in figure legends. Student's unpaired t test was used for two group comparisons. Analyses of multiple groups were performed by a one-way or two-way analysis of variance (ANOVA) followed by post hoc multiple comparisons using Tukey's test. Additional statistical details are given in the figure legends and in the main text. The number of samples N can be found in the figures and in the results.

DATA AND CODE AVAILABILITY

Analysis scripts and data generated by this study are available from the Lead Contact upon request.